arXiv:1510.00771v1 [cs.CV] 3 Oct 2015

Design and Analysis of a Single−Camera Omnistereo Sensor for Quadrotor Micro Aerial Vehicles (MAVs)

Carlos Jaramillo
e−mail: cjaramillo@gradcenter.cuny.edu

October 6, 2015

Abstract

We describe the design and 3D sensing performance of an omnidirectional stereo-vision system (omnistereo) as applied to Micro Aerial Vehicles (MAVs). The proposed omnistereo model employs a monocular camera that is co-axially aligned with a pair of hyperboloidal mirrors (folded catadioptric configuration). We show that this arrangement is practical for performing stereo-vision when mounted on top of propeller-based MAVs characterized by low payloads. The theoretical single viewpoint (SVP) constraint helps us derive analytical solutions for the sensor's projective geometry and generate SVP-compliant panoramic images to compute 3D information from stereo correspondences (in a truly synchronous fashion). We perform an extensive analysis on various system characteristics such as its size, catadioptric spatial resolution, field-of-view. In addition, we pose a probabilistic model for uncertainty estimation of the depth from triangulation for skew back-projection rays. We expect to motivate the reproducibility of our solution since it can be adapted (optimally) to other catadioptric-based omnistereo vision applications.

1 Introduction

1.1 Motivation

Micro aerial vehicles (MAVs), such as quadrotor helicopters, are popular platforms for unmanned aerial vehicle (UAV) research due to their structural simplicity, small form factor, their vertical take-off and landing (VTOL) capability, and high omnidirectional maneuverability. In general, UAVs have plenty of military and civilian applications, such as target localization and tracking, 3-dimensional (3D) mapping, terrain and infrastructural inspection, disaster monitoring, environmental and traffic surveillance, search and rescue, deployment of instrumentation, and cinematography, among other uses. However, with MAVs, their payload and on-board computation limitations constrain their sensors to be compact and lightweight and to execute efficient signal-processing algorithms with data obtained from as few sensors as possible to avoid synchronization delays. The most commonly used perception sensors on MAVs are laser scanners and camera(s) in various configurations such as monocular, stereo, or omnidirectional. Lightweight 2.5D laser scanners like those made by Hokuyo® exist and can accurately measure distances at fast rates, however, they are limited to plane sweeps, which in turn require the quadrotor to move up and down constantly in order to generate full 3D

maps or to foresee obstacles and free space for navigation. More recently, 3D laser/lidar rangefinders have started to emerge, but their size is still an issue for MAVs applications. One last disadvantage of laser rangefinders is their active sensing nature, which consumes more power than cameras and are vulnerable to signal corruption (e.g. due dark/reflective surfaces). Red, green, blue plus depth (RGB-D) sensors like the Microsoft Kinect® are also very popular for 3D navigation, but they have been adopted for mainly indoor navigation [30] due to its structured infrared light projection and short range sensing under 5 m. Hence, a lightweight imaging system of compact structure and capable of providing a large field of view (FOV) instantaneously at acceptable resolutions is necessary for MAV applications in 3D space. These requirements motivate the design and analysis of our omnidirectional stereo (omnistereo) sensor detailed in this manuscript.

1.2 Related Work

In general, stereo vision is used to produce dense or sparse depth maps of the overlapping view instantenously, and its various uses are well known, for example, in 3D reconstruction, in generating occupancy grids for obstacle avoidance, etc., including its application to AUVs [5]. Omnidirectional stereo based on multi-view camera arrangements have also been formulated through the literature. Alternatively, omnidirectional 'catadioptric' vision systems are a possible solution employing cameras and mirrors [9]. Originally, Nayar and Peri [21] studied 9 possible folded configurations for a single-camera omnistereo imaging system. Throughout the years, [17] [2] [6] [26] [19] [22] are some of the works that have implemented various of omnistereo catadioptric configurations for ground mobile robots. Unfortunately, these systems are not compact since they use separate camera-mirror pairs, which it is known to cause synchronization issues. In fact, omnidirectional vision using a single mirror for flying of large UAVs was first attempted in [14]. In [13], Hrabar proposed the use of traditional horizontal stereo-based obstacle avoidance and path planing for AUVs, but these techniques were only tested in a scaled-down air vehicle simulator (AVS). In fact, we believe we are the first to present a single-camera catadioptric approach to omnistereo vision for MAVs. The initial geometry of our model was proposed in [10] and the first prototypes were fabricated in [16].

It is true that a omnidirectional catadioptric system sacrifices spatial resolution on the imaging sensor (as we analyze in Section 3.4). Higher resolution panoramas could be achieved by rotating a linear camera as presented in [23], but this approach has severe disadvantages in dynamic environments. Hence, our sensor offers practical advantages such as reduced cost, weight, and truly-instantaneous pixel-disparity correspondences since a single camera does not introduce extra discrepancies on its intrinsic parameters or mis-synchronization issues. In our previous work [18], we developed a novel omnidirectional omnistereo catadioptric rig consisting of a perspective camera coaxially-aligned with two spherical mirrors of distinct radii (in a "folded" configuration). One caveat of spherical mirrors is their non-centrality as these do not satisfy the single effective viewpoint (SVP) constraint (discussed in Section 2.2). Instead, a locus of viewpoints is obtained rather than the more desirable SVP projection. [27]. Therefore, we extend our research to design a SVP-compliant omnistereo system based on a folded, catadioptric configuration with hyperboloidal mirrors. Yi and Ahuja implemented a few configurations (mixing mirrors and lenses) for omnidirectional stereo vision system using a single camera and capable of a lengthy baseline [31]. In [11], He et al. also implemented a folded catadioptric system with hyperbolic mirrors for wider baseline and they

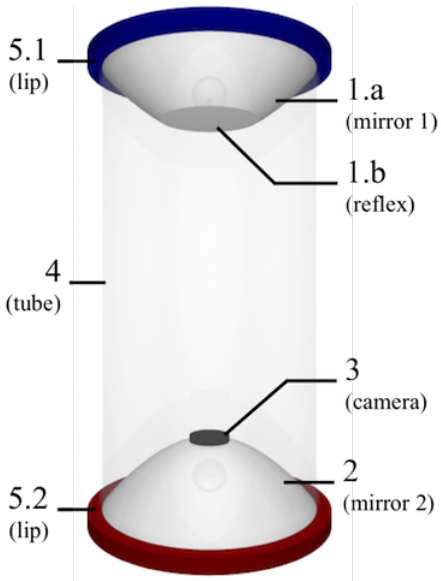

Figure 1: Synthetic catadioptric single-camera omnistereo system, whose main tangible are components: 1.a-b) hyperboloid-planar combined mirror at top, 2) hyperboloidal mirror at bottom, 3) camera, 4) transparent cylindrical support, and 5.1-2) blue-red lips acting as circular markers during image processing.

proposed various solutions to the stereo matching problem for their panoramic images (something not dealt with here, and we refer the reader to [1]). Indeed, our approach resembles the work of Jang, Kim, and Kweon in [15], who also proved the concept for a single camera catadioptric stereo system using hyperbolic mirrors. However, their sensor's characteristics were not analyzed in order to justify their design parameters and capabilities. Actually, we perform an elaborate analysis of our model's parameters (Section 2) involving its geometric projection (Section 3) that are obtained as a constrained numerical optimization solution devising the sensor's real-life application to MAVs passive range sensing (Section 4). We also show how the panoramic images are obtained, where we find correspondences and triangulate 3D points for which an uncertainty model is introduced (Section 5). We finally discuss our experimental results for 3D sensing from omnistereo and discuss future directions of our work (Section 6).

1.3 Symbol Notation

In this subsection, we present the notation style used throughout the remaining of this manuscript:

- With $\mathbb{R}^3$ as the set of all real points in Euclidean 3D space, a point $\mathrm{P}_i \in \mathbb{R}^3$ uses a post-subscript i to be identified from all the other points P, a strict subset of $\mathbb{R}^3$ or symbolically: $P \subset \mathbb{R}^3$ such that $\mathrm{P}_i \bigcup P = \mathbb{R}^3$.

- The origin of a coordinates system or frame is denoted by point O_A, where the subscript indicates the frame's name. In this case, [A] is the reference frame, which we put in square brackets ("[ ]") for clarity. We also name images with this frame notation style.

- The position of a 3D point P_i with respect to a reference frame [A] is indicated component-wise by a column vector of similar name (written in boldface upright lowercase) such as ${}^{[A]}\mathbf{p}_i = [x_i, \quad y_i, \quad z_i]^\mathsf{T}$. Notice how the frame [A], which vector $\mathbf{p}_i$ is referred with respect to, is written as a pre-superscript on a symbol. Using homogeneous coordinates, the same vector is indicated with an h post-subscript as in ${}^{[A]}\mathbf{p}_{i,h} = [x_i, \quad y_i, \quad z_i, \quad 1]^\mathsf{T}$.

- Differing from the 3D vector notation style, the position vector of a 2D point is written in boldface italic lowercase, such as ${}^{[I]}\boldsymbol{m}_i$ for a pixel position on image frame [I].

- As usual, the transpose of a vector or a matrix is indicated by a post-superscript "T" symbol, such as $\mathbf{p}^\mathsf{T}$.

- Double vertical bars ("||") on each side of a vector expression are used to denote its magnitude (Euclidean norm). By definition, $\|\mathbf{p}_i\| = \sqrt{{x_i}^2 + {y_i}^2 + {z_i}^2}$.

- A unit vector wears a caret ("^") on top. For instance, $\hat{\mathbf{q}}$ obeys $\|\hat{\mathbf{q}}\| = 1$.

- Matrices are represented in boldface upright uppercase. A matrix $\mathbf{M}_i$ will be written as $\mathbf{M}_{i,h}$ in homogeneous coordinates.

- Function names use upright lowercase letters and additional subscript names based on context. To distinguish vector-valued functions from scalar-valued functions, we use boldface, such as for the backward projection function $\mathbf{f}_\beta$.

2 Sensor Design

Figure 1 shows the single-camera catadioptric omnistereo vision system that we specifically design to be mounted on top of our micro quadrotors (manufactured by Ascending Technologies [28]). It consists of 1) one hyperboloid-planar mirror at the top, 2) one hyperboloidal mirror at the bottom, and 3) a high-resolution USB camera also at the bottom (inside the bottom mirror and looking up). The components are housed and supported by a 4) transparent tube or plastic standoffs (for the real-life prototype shown in Figure 13). The circular lips (5.1-2) that extend out of each mirror are respectively colored blue and red and serve to assist with the boundary recognition during calibration (not discussed in this work). The choice of the hyperboloidal reflectors owes to three reasons: it is one of the four non-degenerated conic shapes satisfying the SVP constraint [3]; it allows a wider vertical FOV than elliptical and planar mirrors; and it does not require a telescopic (orthographic) lens for imaging as with paraboloidal mirrors (so our system can be downsized). In addition, the planar part of mirror 1 works as a reflex mirror, which in part reduces distortion caused by dual conic reflections. Based on the SVP property, the system obtains two radial images of the omnidirectional views in the form of an inner and an outer ring as illustrated in Figure 2a and Figure 2b). Nevertheless, the unique

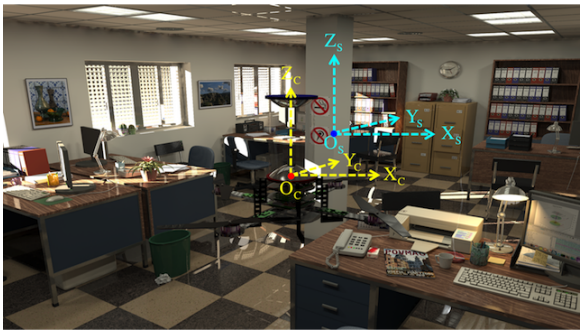

(a) External view

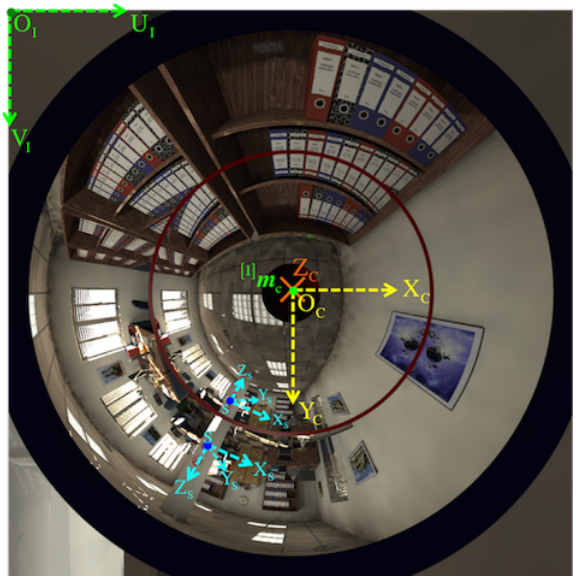

(b) Camera view

Figure 2: Photo-realistic synthetic scene: **(a)** Side-view of the quadrotor with the omnistereo rig in an office environment (the scene frame [S] and the system camera frame [C] can be appreciated). **(b)** the image captured by the system's camera using the same pose shown in Figure 2a's scene. O_I is the origin of the image frame [I] and is located at the top-left corner, whereas the camera frame [C] coincides with the image's center point $^{[I]}\boldsymbol{m}_c$. Here, the camera's optical axis is coincident with the $+Z_C$-axis, which is perpendicularly directed into the virtual image plane π. Notice how objects reflected by the bottom mirror appear in the inner image ring bounded by a red circle mark, whereas reflections from the top mirror are imaged in the outer ring. Radial correspondences of pixels around the image's center facilitate the computation of depth explained in (Section 5).

set of parameters describing the entire system categorizes it as a "global camera model" given by [25] because changing the value of any parameter in the model affects the overall projection function of visible light rays in the scene (imaging) as well as other computational imaging factors such as depth resolution and overlapping field of view, which we attempt to optimize with the following design subsections.

2.1 Model Parameters

In the configuration of Figure 3, mirror 1's real or primary focus is F_1, which is separated by a distance c_1 from its virtual or secondary focus, F_1', at the bottom. Without loss of generality, we make both the camera's pinhole and F_1' coincide with the origin of the camera's coordinate system, $\mathrm{O_C}$. This way, the position of the primary focus, F_1, can be referenced by vector ${}^{[\mathrm{C}]}\mathbf{f}_1 = [0, \quad 0, \quad c_1]^\mathsf{T}$ in Cartesian coordinates with respect to the camera frame, [C]. Similarly, the distance between the foci of mirror 2, F_2 and F_2', is measured by c_2. Here, we use the planar (reflex) mirror of radius r_{ref} and unit normal vector

$$ {}^{[\mathrm{C}]}\hat{\mathbf{n}}_{ref} = [0, \quad 0, \quad -1] \tag{2.1} $$

in order to project the real camera's pinhole located at $\mathrm{O_C}$ as a virtual camera $\mathrm{O_C}'$ coinciding with the virtual focal point F_2' positioned at ${}^{[\mathrm{C}]}\mathbf{f}_{2v} = [0, \quad 0, \quad d]^\mathsf{T}$. We achieve this by setting $d/2$ as the symmetrical distance from the reflex mirror to $\mathrm{O_C}$ and from the reflex mirror to $\mathrm{O_C}'$. With respect to [C], mirror 2's primary focus, F_2, results in position ${}^{[\mathrm{C}]}\mathbf{f}_2 = [0, \quad 0, \quad d - c_2]^\mathsf{T}$. It yields the following expression for the reflective plane:

$$ {}^{[\mathrm{C}]}\hat{\mathbf{n}}_{ref}^\mathsf{T}\,{}^{[\mathrm{C}]}\mathbf{x} = -d/2 \tag{2.2} $$

The profile of each hyperboloid is determined by independent parameters k_1 and k_2, respectively. Their reflective vertical field of view (vFOV) are indicated by angles α_1 and α_2. They play an important role when designing the total vFOV of the system, α_{sys}, formally defined by equation (3.33) and illustrated in Figure 5. Also importantly, while performing stereo vision, it is to consider angle α_{SROI}, which measures the common (overlapping) vFOV of the omnistereo system. The camera's nominal field of view α_{cam} and its opening radius r_{cam} also determine the physical areas of the mirrors that can be fully imaged. Theoretically, the mirrors' vertical axis of symmetry (coaxial configuration) produces two image points that are radially collinear. This property is advantageous for the correspondence search during stereo sensing (Section 5) with a baseline measured as

$$ b = |c_1 + c_2 - d| \tag{2.3} $$

Among design parameters, we also include the total height of the system, h_{sys}, and its weight m_{sys}, both being formulated in Section 2.3.

To summarize, the model has 6 primary design parameters given as a vector

$$ \boldsymbol{\theta} = \begin{bmatrix} c_1, & c_2, & k_1, & k_2, & d, & r_{sys} \end{bmatrix} \tag{2.4} $$

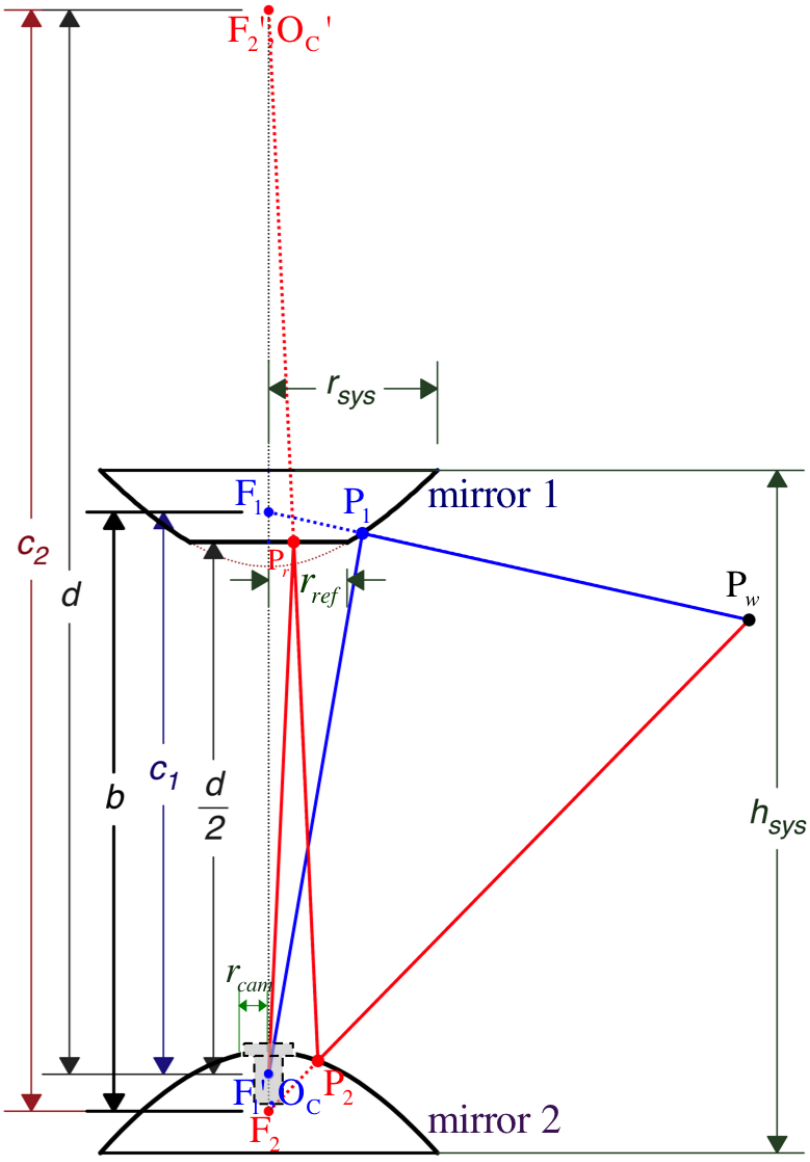

Figure 3: 2D cross-section of the geometric model and dimension lines for observable constraint parameters: $c_1, c_2, d, r_{sys}, r_{ref}, r_{cam}$; and relevant by-product parameters: baseline b and system height h_{sys}. In addition, the projection paths corresponding to a world point P_w are also traced in route to the mirrors real foci, F_1 and F_2, and their respective reflection points, P_1 and P_2, to the real pinhole camera O_C. Notice the equivalent projection of P_2 via the virtual camera $O_C{}'$ achieved by the reflex mirror located at distance $d/2$ from O_C.

in addition to by-product parameters such as

$$\Big[b, \quad h_{sys}, \quad r_{ref}, \quad r_{cam}, \quad m_{sys}, \quad \alpha_1, \quad \alpha_2, \quad \alpha_{sys}, \quad \alpha_{SROI}, \quad \alpha_{cam}\Big].$$

In Section 4, we perform a numerical optimization of the parameters in $\boldsymbol{\theta}$ with the goal to maximize the baseline, b, required for life-size navigational stereopsis. At the same time, we restrict the overall size of the rig (Section 2.3) without sacrificing sensing performance characteristics such as vertical field of view, spatial resolution, and depth resolution. In the upcoming subsections, we first derive the analytical solutions for the forward projection problem in our coaxial stereo configuration as a whole. In Section 3.2, we derive the back-projection equations for lifting 2D image points into 3D space (up to scale).

2.2 Single Viewpoint (SVP) Configuration for OmniStereo

As a central catadioptric system, its projection geometry must obey the existence of the so-called single effective viewpoint (SVP). While the SVP guarantees that true perspective geometry can always be recovered from the original image, it limits the selection of mirror profiles to a set of conic sections [2]. Generally, a circular hyperboloid of revolution (about its axis of symmetry) conforms to the SVP constraint as demonstrated by Baker and Nayar in [20]. Since a hyperboloidal mirror has two foci, the effective viewpoint is the primary focus F inside the physical mirror and the secondary (outer) focus F$'$ is where the centre (pinhole) of the perspective camera should be placed for depicting a scene obeying the SVP configuration discussed in this section.

First of all, a hyperboloid i can be described by the following parametric equation:

$$\frac{\big(z_i - z_{0_i}\big)^2}{a_i^2} - \frac{r_i^2}{b_i^2} = 1, \text{ with } a_i = \frac{c_i}{2}\sqrt{\frac{k_i - 2}{k_i}}, \; b_i = \frac{c_i}{2}\sqrt{\frac{2}{k_i}} \tag{2.5}$$

where the only two parameters are $z_{0_i} = \frac{c_i}{2}$, the offset (shift) position of the focus along the Z-axis from the origin $\mathrm{O_C}$, and r_i is the orthogonal distance to the axis of revolution / symmetry (i.e. the Z-axis) from a point P_i on its surface.

In fact, the position of a valid point P_i is constrained within the mirror's physical surface of reflection, which is radially limited by $r_{i,min}$ and $r_{i,max}$, such that:

$$r_i = \sqrt{x_i^2 + y_i^2}, \;\; \text{for} \;\; r_{i,min} \leq r_i \leq r_{i,max}, \; \forall i \in \{1,2\} \tag{2.6}$$

and $r_{1,min} = r_{ref}$, $r_{1,max} = r_{sys}$, $r_{2,min} = r_{cam}$, $r_{2,max} = r_{sys}$. Observe that the radius of the system is the upper bound for both mirrors (Figure 3). In addition, the hyperboloids profiled by equation (2.5) must obey the following conical constraints:

$$\forall i \in \{1,2\} \, (c_i > 0 \wedge k_i > 2) \tag{2.7}$$

k is a constant parameter (unit-less) inversely related to the mirror's curvature or more precisely, the eccentricity ε_c of the conic. In fact, $\varepsilon_c > 1$ for hyperbolas, yet a plane is produced when $\varepsilon_c \to \infty$ or $k = 2$.

We devise M_i as the set of all the reflection points P_i with coordinates (x_i, y_i, z_i) laying on the surface of the respective mirror i within bounds. Formally,

$$M_i := \left\{ \mathrm{P}_i \in \mathbb{R}^3 \;\middle|\; \frac{\left(z_i - z_{0_i}\right)^2}{a_i^2} - \frac{r_i^2}{b_i^2} = 1 \wedge \text{Eq.(2.6)} \wedge \text{Eq.(2.7)} \right\} \tag{2.8}$$

In our model, we describe both hyperboloidal mirrors, 1 and 2, with respect to the camera frame [C], which acts as the common origin of the coordinates system. Therefore,

$$z_{0_1} = \frac{c_1}{2} \tag{2.9}$$

$$z_{0_2} = d - \frac{c_2}{2} \tag{2.10}$$

By expanding equation (2.5) with their respective index terms, it becomes

$$\left(z_1 - \frac{c_1}{2}\right)^2 - r_1^2\left(\frac{k_1}{2} - 1\right) = \frac{c_1^2}{4}\left(\frac{k_1 - 2}{k_1}\right) \tag{2.11}$$

$$\left(z_2 - d + \frac{c_2}{2}\right)^2 - r_2^2\left(\frac{k_2}{2} - 1\right) = \frac{c_2^2}{4}\left(\frac{k_2 - 2}{k_2}\right) \tag{2.12}$$

Additionally, we define the function $\mathrm{f}_{z_i} : r \mapsto z_i$ to find the corresponding z_i component from a given r value as

$$\mathrm{f}_{z_i}(r) := \begin{cases} z_{0_i} + \gamma_i & \text{if } i = 1 \wedge \text{Eq.(2.6)}, \\ z_{0_i} - \gamma_i & \text{if } i = 2 \wedge \text{Eq.(2.6)}, \\ \mathit{None} & \text{otherwise.} \end{cases} \tag{2.13}$$

where $\gamma_i = \dfrac{a_i}{b_i}\sqrt{b_i^2 + r_i^2}$.

The inverse relation $\mathrm{f}_{r_i} : z \mapsto \{+r_i, -r_i\}$ can be also implemented as

$$\mathrm{f}_{r_i}(z) := \begin{cases} \pm b_i \Gamma_i & \text{if } i \in \{1,2\} \wedge \text{Eq.(2.6)}, \\ \mathit{None} & \text{otherwise.} \end{cases} \tag{2.14}$$

where $\Gamma_i = \sqrt{\dfrac{\left(z - z_{0_i}\right)^2}{a_i^2} - 1}$, so a valid input z can be associated with both positive and negative solutions r_i.

2.3 Rig Size

In the attempt to evaluate the overall system size, we consider the height and weight variables due to the primary design parameters, $\boldsymbol{\theta}$.

First, the height of the system, h_{sys} can be estimated from the functional relationships f_{z_1} and f_{z_2} defined in equation (2.13), which can provide the respective $z-$component values at the out-most point on the mirror's surface. More specifically, knowing r_{sys}, we get

$$h_{sys} = z_{max} - z_{min} \tag{2.15}$$

where $z_{max} = \mathrm{f}_{z_1}(r_{sys})$ and $z_{min} = \mathrm{f}_{z_2}(r_{sys})$.

The rig's weight can be indicated by the total resulting mass of the main "tangible" components:

$$m_{sys} = m_{cam} + m_{tub} + m_{mir} \tag{2.16}$$

where the mass of the camera-lens combination is m_{cam}; the mass of the support tube can be estimated from its cylindrical volume V_{tub} and material density ρ_{tub}, and the mass due to the mirrors

$$\begin{aligned} m_{mir} &= V_{mir}\rho_{mir} \\ &= \left(V_1 + V_{ref} + V_2\right)\rho_{mir} \end{aligned} \tag{2.17}$$

For computing the volume of the hyperboloidal shell, V_i for mirror i, we apply a "ring method" of volume integration. By assuming all mirror material has the same wall thickness τ_m, we acquire V_i by integrating the horizontal cross-sections area along the Z-axis. Each ring area depends on its outer and inner circumferences that vary according to radius $r\,|_z$ for a given height z. Equation (2.14) establishes the functional relation ${r_i}^+ = \mathrm{f}_{r_i}(z)$, from which we only need its positive answer. We let A be the function that computes the ring area of constant thickness τ_m for a variable outer radius r_i

$$\begin{aligned} A(r_i) &= \pi r_i^2 - \pi\left(r_i - \tau_m\right)^2 \\ &= \pi\tau_m\left(2r_i - \tau_m\right) \end{aligned} \tag{2.18}$$

We consider the definite integral evaluated in the z interval bounded by its height limits, which are correlated with its radial limits equation (2.6) and can be obtained via the f_{z_i} defined in equation (2.13), such that

$$z_{i,min} = \mathrm{f}_{z_i}\left(r_{i,min}\right) \quad \text{and} \quad z_{i,max} = \mathrm{f}_{z_i}\left(r_{i,max}\right) \tag{2.19}$$

Then, we proceed to integrate equation (2.18), so the shell volume for each hyperboloidal mirror is defined as

$$V_i = \int_{z_{i,min}}^{z_{i,max}} A(r_i)\,\mathrm{d}z \tag{2.20}$$

Finally, since the reflex mirror piece is just a solid cylinder of thickness τ_m, its volume is simply

$$V_{ref} = \tau_m \pi r_{ref}^2 \tag{2.21}$$

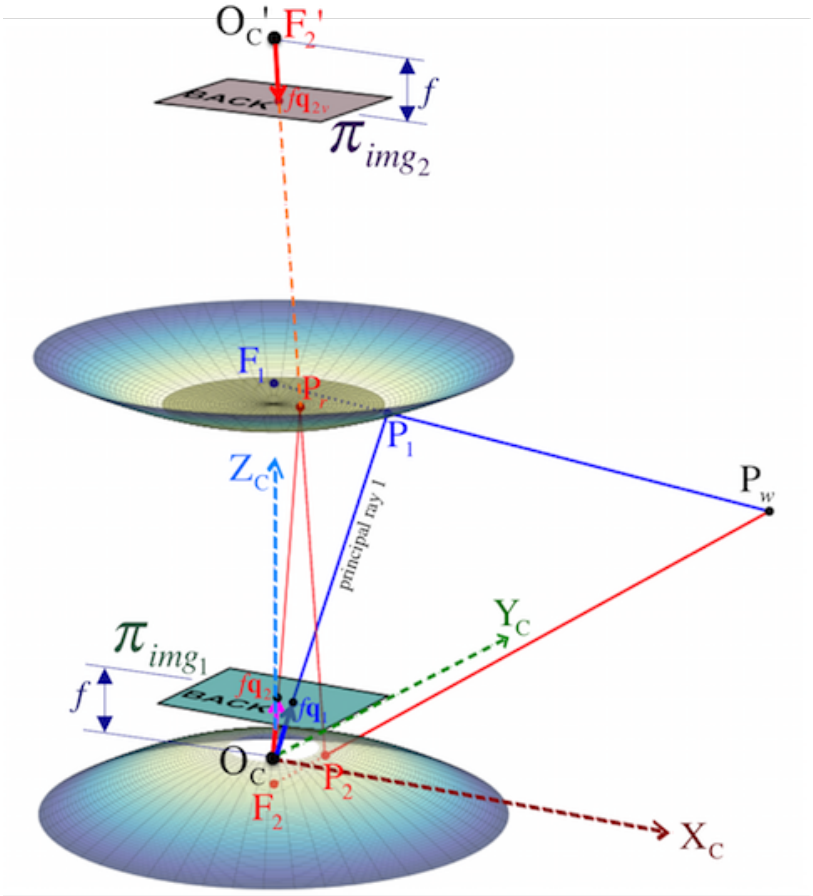

Figure 4: Omnistereo image formation. A 3D point P_w is ray-traced as to produce 2D image points (pixels): ${}^{[I]}\boldsymbol{m}_1$ due to reflection on mirror 1, and ${}^{[I]}\boldsymbol{m}_2$ due to reflection on mirror 2 via the planar (reflex) mirror. Although the one-and-only imaging sensor is the camera plane π_{cam} , we conveniently imagine two virtual projection planes π_{img_1} and π_{img_2}, where the latter presumes to capture points reflecting on mirror 2 as if they could pass through the reflex mirror toward the virtual camera $O_C{}'$. The figure does not show the pixel points ${}^{[I]}\boldsymbol{m}_i$ and instead it draws the corresponding vectors $f^{[C]}\mathbf{q}_i$ to the points on the projection plane.

3 Projective Geometry

3.1 Analytical Solutions to Projection (Forward)

Assuming a central catadioptric configuration for the mirrors and camera system (Section 2.2), we derive the closed-form solution to the imaging process (forward projection) for an observable point P_w, positioned in three-dimensional Euclidean space, $\mathbb{R}^3$, with respect to the reference frame, [C], as vector ${}^{[\mathrm{C}]}\mathbf{p}_w = [x_w, \quad y_w, \quad z_w]^\mathsf{T}$. In addition, we assume all reference frames such as $[\mathrm{F}_1]$ and $[\mathrm{F}_2]$ have the same orientation as [C].

For mathematical stability, we must constrain that all projecting world points lie outside the mirror's volume:

$$\mathrm{f}_{r_i}(z_w) < \rho_w, \text{ where } \rho_w = \sqrt{x_w^2 + y_w^2} \tag{3.1}$$

where f_{r_i} is defined by equation (2.14) and ρ_w measures the horizontal range to P_w.

P_w is imaged at pixel position ${}^{[\mathrm{I}]}\boldsymbol{m}_1$ after its reflection as point P_1 on the hyperboloidal surface of mirror 1 (Figure 4). On the other hand, the second image point's position, ${}^{[\mathrm{C}]}\boldsymbol{m}_2$, due to reflection point P_2 on mirror 2 is rather obtained indirectly after an additional point P_r is reflected at ${}^{[\mathrm{C}]}\mathbf{p}_{ref}$ on the reflex mirror represented via equation (3.11).

First, for P_w's reflection point via mirror 1 at position vector ${}^{[\mathrm{C}]}\mathbf{p}_1$, we use λ_1 as the parametrization term for the line equation passing through F_1 toward P_w with direction ${}^{[\mathrm{F}_1]}\mathbf{d}_1 = {}^{[\mathrm{C}]}\mathbf{p}_w - {}^{[\mathrm{C}]}\mathbf{f}_1$. The position of any point P_1 on this line is given by:

$${}^{[\mathrm{C}]}\mathbf{p}_1 = {}^{[\mathrm{C}]}\mathbf{f}_1 + \lambda_1 {}^{[\mathrm{F}_1]}\mathbf{d}_1 \tag{3.2}$$

Substituting equation (3.2) into equation (2.11), we obtain:

$$\left(\lambda_1(z_w - c_1) + \frac{c_1}{2}\right)^2 - \left(\lambda_1^2 x_w^2 + \lambda_1^2 y_w^2\right)\left(\frac{k_1}{2} - 1\right) - \frac{c_1^2}{4}\left(\frac{k_1 - 2}{k_1}\right) = 0$$

in order to solve for λ_1, which turns out to be

$$\lambda_1 = \frac{c_1}{\left\|{}^{[\mathrm{F}_1]}\mathbf{d}_1\right\| \sqrt{k_1 \cdot (k_1 - 2)} - k_1 (z_w - c_1)} \tag{3.3}$$

where $\left\|{}^{[\mathrm{F}_1]}\mathbf{d}_1\right\| = \sqrt{x_w^2 + y_w^2 + (z_w - c_1)^2}$ is the Euclidean norm between P_w and mirror 1's focus, F_1.

In practice, we represent the reflection point's position ${}^{[\mathrm{C}]}\mathbf{p}_1$ as a matrix-vector multiplication between the 3×4 transformation matrix $\mathbf{K}_1 = [\lambda_1 \mathbf{I}_{(3)}, \quad (1 - \lambda_1)\,{}^{[\mathrm{C}]}\mathbf{f}_1]$ and the point's position vector ${}^{[\mathrm{C}]}\mathbf{p}_{w,h} = [x_w, \quad y_w, \quad z_w, \quad 1]^\mathsf{T}$ in homogeneous coordinates:

$${}^{[\mathrm{C}]}\mathbf{p}_1 = \mathbf{K}_1 {}^{[\mathrm{C}]}\mathbf{p}_{w,h} \tag{3.4}$$

Note that ${}^{[C]}\mathbf{p}_1$'s elevation angle, θ_1, must be bounded as

$$\theta_{1,min} \leq \theta_1 \leq \theta_{1,max} \tag{3.5}$$

where $\theta_{1,min}$ and $\theta_{1,max}$ are the angular elevation limits for the real reflective area of the hyperboloid.

Finally, the reflection point P_1 with position ${}^{[C]}\mathbf{p}_1$ can now be perspectively projected as a pixel point located at ${}^{[I]}\boldsymbol{m}_1 = [u_1, \quad v_1]^\mathsf{T}$ on the image. In fact, the entire imaging process of P_w via mirror 1 can be expressed in homogeneous coordinates as:

$${}^{[I]}\boldsymbol{m}_{1,h} = \zeta_1 \mathbf{K}_c \mathbf{K}_1 {}^{[C]}\mathbf{p}_{w,h} \tag{3.6}$$

where the scalar $\zeta_1 = 1/z_1 = 1/\left(c_1 + \lambda_1 (z_w - c_1)\right)$ is the perspective normalizer that maps the *principal ray* passing through $\mathbf{p}_1$ onto a point ${}^{[C]}\mathbf{q}_1 = [x_{q_1}, \quad y_{q_1}, \quad 1]^\mathsf{T}$ on the normalized projection plane $\hat{\pi}_{img_1}$. The traditional 3×3 intrinsic matrix of the camera's pinhole model is

$$\mathbf{K}_c = \begin{bmatrix} f_u & s & u_c \\ 0 & f_v & v_c \\ 0 & 0 & 1 \end{bmatrix} \tag{3.7}$$

in which $f_u = f/h_x$ and $f_v = f/h_y$ are based on the focal length f and the pixel dimension (h_x, h_y), s is the skew parameter, and ${}^{[I]}\boldsymbol{m}_c = [u_c, \quad v_c]^\mathsf{T}$ is the optical center position on the image [I] Figure 4 illustrates the projection point $f^{[C]}\mathbf{q}_1$ on the respective image plane π_{img_1}.

Similarly, we provide the analytical solution for the forward projection of P_w via mirror 2 by first considering the position of reflection point P_2:

$${}^{[C]}\mathbf{p}_2 = \mathbf{K}_2 {}^{[C]}\mathbf{p}_{w,h} \tag{3.8}$$

where $\mathbf{K}_2 = [\lambda_2 \mathbf{I}_{(3)}, \quad (1-\lambda_2) {}^{[C]}\mathbf{f}_2]$ is similar to the transformation matrix $\mathbf{K}_1$, but obviously it now uses ${}^{[C]}\mathbf{f}_2$ and

$$\lambda_2 = \frac{c_2}{\left\| {}^{[F_2]}\mathbf{d}_2 \right\| \sqrt{k_2 \cdot (k_2 - 2)} + k_2 \left(z_w - (d - c_2)\right)} \tag{3.9}$$

with direction vector's norm

$$\left\| {}^{[F_2]}\mathbf{d}_2 \right\| = \left\| {}^{[C]}\mathbf{p}_w - {}^{[C]}\mathbf{f}_2 \right\| = \sqrt{x_w^2 + y_w^2 + \left(z_w - (d - c_2)\right)^2} \tag{3.10}$$

For completeness, note that the physical projection via mirror 2 is incident to the reflex mirror at

$${}^{[C]}\mathbf{p}_{ref} = {}^{[C]}\mathbf{f}_{2v} + \lambda_{ref} \left({}^{[C]}\mathbf{p}_2 - {}^{[C]}\mathbf{f}_{2v} \right) \tag{3.11}$$

where $\lambda_{ref} = \frac{d}{2(d - z_2)}$ according to equation (2.2) in the theoretical model. Ultimately, ignoring any astigmatism and chromatic aberrations introduced by the reflex mirror, and because the same (and only) real camera with $\mathbf{K}_c$ is used for imaging, we obtain the projected pixel position ${}^{[I]}\boldsymbol{m}_{2,h} = [u_2, \quad v_2, \quad 1]^\mathsf{T}$ in homogeneous coordinates:

$${}^{[I]}\boldsymbol{m}_{2,h} = \zeta_2 \mathbf{K}_c \mathbf{M}_{ref} \mathbf{K}_2 {}^{[C]}\mathbf{p}_{w,h} \tag{3.12}$$

where $\zeta_2 = 1/(d - z_2)$ is the perspective normalizer to find ${}^{[\mathrm{C}]}\mathbf{q}_2$ on the normalized projection plane, $\hat{\pi}_{img_2}$.

Due to planar mirroring via the reflex mirror, ${}^{[\mathrm{C}']}_{[\mathrm{C}]}\mathbf{M}_{ref}$ is used to change the coordinates of P_2 from [C] onto the virtual camera frame, $[\mathrm{C}']$, located at ${}^{[\mathrm{C}]}\mathbf{f}_{2v}$. Hence,

$$ {}^{[\mathrm{C}']}_{[\mathrm{C}]}\mathbf{M}_{ref} = \left[\mathbf{I}_{(3)} + 2\mathbf{D}_{\hat{\mathbf{n}}_{ref}}, \qquad {}^{[\mathrm{C}]}\mathbf{f}_{2v}\right] \tag{3.13} $$

where the 3×1 unit normal vector of the reflex mirror plane, ${}^{[\mathrm{C}]}\hat{\mathbf{n}}_{ref}$ given in (2.1), is mapped into its corresponding 3×3 diagonal matrix $\mathbf{D}_{\hat{\mathbf{n}}_{ref}}$, via the relationship:

$$ \mathbf{D}_{\hat{\mathbf{n}}_{ref}} \leftarrow \mathbf{I}_{(3)}\mathrm{diag}\left({}^{[\mathrm{C}]}\hat{\mathbf{n}}_{ref}\right) \tag{3.14} $$

It is convenient to define the forward projection functions $\mathbf{f}_{\varphi_1}({}^{[\mathrm{C}]}\mathbf{p})$ and $\mathbf{f}_{\varphi_2}({}^{[\mathrm{C}]}\mathbf{p})$ for a 3D point P whose position vector is known with respect to [C] and which is situated within the vertical field of view α_i of mirror i (for $i \in \{1,2\}$) indicated in Figure 5. The respective function $\mathbf{f}_{\varphi_i}({}^{[\mathrm{C}]}\mathbf{p})$ maps to image point ${}^{[\mathrm{I}]}\boldsymbol{m}_i$ on frame [I], such that $\mathbf{f}_{\varphi_i} : \mathbb{R}^3 \mapsto \mathbb{R}^2$ and implemented as:

$$ \mathbf{f}_{\varphi_i}({}^{[\mathrm{C}]}\mathbf{p}) := \begin{cases} {}^{[\mathrm{C}]}\mathbf{p} \xrightarrow{\text{Eq. (3.6)}} {}^{[\mathrm{I}]}\boldsymbol{m}_1 & \text{if } i = 1 \wedge \text{ Eqs. (3.16)(3.1)}, \\ {}^{[\mathrm{C}]}\mathbf{p} \xrightarrow{\text{Eq. (3.12)}} {}^{[\mathrm{I}]}\boldsymbol{m}_2 & \text{if } i = 2 \wedge \text{ Eqs. (3.16)(3.1)}, \\ None & \text{otherwise.} \end{cases} \tag{3.15} $$

In fact, ${}^{[\mathrm{I}]}\boldsymbol{m}_i$ is considered valid if it is located within the imaged radial bounds, such that:

$$ {}^{[\mathrm{I}_{\mathrm{C}_i}]}\left\|{}^{[\mathrm{I}]}\boldsymbol{m}_{r_{i,min}}\right\| \;\leq\; {}^{[\mathrm{I}_{\mathrm{C}_i}]}\left\|{}^{[\mathrm{I}]}\boldsymbol{m}_i\right\| \;\leq\; {}^{[\mathrm{I}_{\mathrm{C}_i}]}\left\|{}^{[\mathrm{I}]}\boldsymbol{m}_{r_{i,max}}\right\| \tag{3.16} $$

where the frame of reference $[\mathrm{I}_{\mathrm{C}_i}]$ implies that its origin is the image center ${}^{[\mathrm{I}_i]}\boldsymbol{m}_c = [u_{c_i}, \quad v_{c_i}]^{\mathsf{T}}$ of the $[\mathrm{I}_i]$ masked imaged. Therefore, the magnitude (norm) of any position ${}^{[\mathrm{I}_{\mathrm{C}_i}]}\boldsymbol{m}$ in pixel space $[\mathrm{I}_{\mathrm{C}_i}]$ can be measured as

$$ {}^{[\mathrm{I}_{\mathrm{C}_i}]}\left\|{}^{[\mathrm{I}_i]}\boldsymbol{m}\right\| := \left\|{}^{[\mathrm{I}_i]}\boldsymbol{m} - {}^{[\mathrm{I}_i]}\boldsymbol{m}_c\right\| = \sqrt{(u-u_c)^2 + (v-v_c)^2} \tag{3.17} $$

In particular, ${}^{[\mathrm{I}_{\mathrm{C}_i}]}\left\|{}^{[\mathrm{I}]}\boldsymbol{m}_{r_{i,lim}}\right\|$ is the image radius obtained from the projection ${}^{[\mathrm{I}]}\boldsymbol{m}_{r_{i,lim}} \leftarrow \mathbf{f}_{\varphi_i}({}^{[\mathrm{C}]}\mathbf{p}_{i,lim})$ corresponding to a particular point coincident with the line of sight of the radial limit $r_{i,lim}$ – it being either r_{sys}, r_{ref}, or r_{cam} as indicated by equation (2.6).

3.2 Analytical Solutions to Back Projection

The back projection procedure establishes the relationship between the 2D position of a pixel point ${}^{[\mathrm{I}]}\boldsymbol{m} = [u, \quad v]^{\mathsf{T}}$ on the image [I] and its corresponding 3D projective direction vector $\mathbf{v}$ toward the observed point P_w in the world.

Initially, the pixel point ${}^{[\mathrm{I}]}\boldsymbol{m}_1$ (imaged via mirror 1) is mapped as Q_1 onto the normalized projection plane $\hat{\pi}_{img_1}$ with coordinates ${}^{[\mathrm{C}]}\mathbf{q}_1 = [x_{q_1}, \quad y_{q_1}, \quad 1]^{\mathsf{T}}$ by applying the inverse transformation of the camera intrinsic matrix equation (3.7) as follows:

$$ {}^{[\mathrm{C}]}\mathbf{q}_1 = {}^{[\mathrm{C}]}_{[\mathrm{I}]}\mathbf{K}_c^{-1\,[\mathrm{I}]}\mathbf{m}_{1,h} = \begin{bmatrix} \frac{1}{f_u} & -\frac{s}{f_u f_v} & \frac{s v_c - f_v u_c}{f_u f_v} \\ 0 & \frac{1}{f_v} & -\frac{v_c}{f_v} \\ 0 & 0 & 1 \end{bmatrix} \begin{bmatrix} u_1 \\ v_1 \\ 1 \end{bmatrix} \tag{3.18} $$

For simplicity, we assume no distortion parameters exist, so we can proceed with the lifting step along the principal ray that passes through three points: the camera's pinhole $\mathrm{O_C}$, point Q_1 on the projection plane, and the reflection point P_1 (Figure 4). The vector form of this line equation can be written as:

$$ {}^{[\mathrm{C}]}\mathbf{p}_1 = {}^{[\mathrm{C}]}\mathbf{o}_c + t_1\left({}^{[\mathrm{C}]}\mathbf{q}_1 - {}^{[\mathrm{C}]}\mathbf{o}_c\right) = t_1\,{}^{[\mathrm{C}]}\mathbf{q}_1 \tag{3.19} $$

By substituting equation (3.19) into (2.11), we solve for the parameter t_1, to get

$$ t_1 = \frac{c_1}{k_1 - \left\|{}^{[\mathrm{C}]}\mathbf{q}_1\right\|\sqrt{k_1 \cdot (k_1 - 2)}} \tag{3.20} $$

where $\left\|{}^{[\mathrm{C}]}\mathbf{q}_1\right\| = \sqrt{x_{q_1}^2 + y_{q_1}^2 + 1}$ is the distance between Q_1 and $\mathrm{O_C}$.

Given ${}^{[\mathrm{F}_1]}\mathbf{v}_1$ as the direction vector leaving focal point F_1 toward the world point ${}^{[\mathrm{C}]}\mathrm{P}_w$. Through frame transformation ${}^{[\mathrm{F}_1]}_{[\mathrm{C}]}T_1\,{}^{[\mathrm{C}]}\mathbf{p}_{1,h}$, we get

$$ {}^{[\mathrm{F}_1]}\mathbf{v}_1 = {}^{[\mathrm{F}_1]}_{[\mathrm{C}]}T_1\,{}^{[\mathrm{C}]}\mathbf{p}_{1,h} \text{ , where } {}^{[\mathrm{F}_1]}_{[\mathrm{C}]}T_{1\,(3\times4)} = \begin{bmatrix} \mathbf{I}_{(3)}, & -{}^{[\mathrm{C}]}\mathbf{f}_1 \end{bmatrix} \tag{3.21} $$

for ${}^{[\mathrm{C}]}\mathbf{p}_{1,h}$ as the homogeneous form of (3.19). In fact, ${}^{[\mathrm{F}_1]}\mathbf{v}_1$ provides the back-projected angles (elevation θ_1, azimuth ψ_1) from focus F_1 toward ${}^{[\mathrm{C}]}\mathrm{P}_w$:

$$ {}^{[\mathrm{F}_1]}\theta_1 = \arcsin\left(\frac{z_{\mathbf{v}_1}}{\left\|{}^{[\mathrm{F}_1]}\mathbf{v}_1\right\|}\right) = \arcsin\left(\frac{z_1 - c_1}{\left\|{}^{[\mathrm{F}_1]}\mathbf{v}_1\right\|}\right) \tag{3.22} $$

$$ {}^{[\mathrm{F}_1]}\psi_1 = \arctan\left(\frac{y_{\mathbf{v}_1}}{x_{\mathbf{v}_1}}\right) = \arctan\left(\frac{y_1}{x_1}\right) \tag{3.23} $$

where $\left\|{}^{[\mathrm{F}_1]}\mathbf{v}_1\right\|$ is the norm of the back-projection vector up to the mirror surface.

Using the same approach, we lift a pixel point ${}^{[\mathrm{I}]}\boldsymbol{m}_2$ imaged via mirror 2. Because the virtual camera $\mathrm{O_C}'$ located at ${}^{[\mathrm{C}]}\mathbf{f}_2 = [0, \quad 0, \quad d - c_2]^{\mathsf{T}}$ uses the same intrinsic matrix $\mathbf{K}_c$, we can safely back-project pixel ${}^{[\mathrm{I}]}\boldsymbol{m}_2$ to Q_{2v} on the normalized projection plane $\hat{\pi}_{img_2}$ as follows:

$$ {}^{[\mathrm{C}']}\mathbf{q}_{2v} = {}^{[\mathrm{C}]}\mathbf{q}_2 = \mathbf{K}_c^{-1\,[\mathrm{I}]}\boldsymbol{m}_{2,h} \tag{3.24} $$

where the inverse transformation of the camera intrinsic matrix $\mathbf{K}_c^{-1}$ is given by equation (3.7). Since the reflection matrix $\mathbf{M}_{ref}$ defined in equation (3.13) is bidirectional due to the symmetric position of the reflex mirror about [C] and $[\mathrm{C}']$, we can find the desired position of ${}^{[\mathrm{C}]}\mathbf{q}_{2v}$ with respect to [C]:

$$ {}^{[\mathrm{C}]}\mathbf{q}_{2v} = {}^{[\mathrm{C}]}_{[\mathrm{C}']}\mathbf{M}_{ref}\,{}^{[\mathrm{C}']}\mathbf{q}_{2v,h} \tag{3.25} $$

which is equivalent to ${}^{[C]}\mathbf{q}_{2v} = [x_{q_{2v}}, \quad y_{q_{2v}}, \quad d-1]^{\mathsf{T}}$.

In Figure 4, we can see the principal ray that passes through the virtual camera's pinhole $O_C{}'$ and the reflection point P_2, so this line equation can be written as:

$$ {}^{[C]}\mathbf{p}_2 = {}^{[C]}\mathbf{f}_{2v} + t_2 \left({}^{[C]}\mathbf{q}_{2v} - {}^{[C]}\mathbf{f}_{2v} \right) \tag{3.26} $$

Solving for t_2 from equation (3.26) and (2.12), we get

$$ t_2 = \frac{c_2}{k_2 - \left\| {}^{[C]}\mathbf{q}_2 \right\| \sqrt{k_2 \cdot (k_2 - 2)}} \tag{3.27} $$

where $\left\| {}^{[C]}\mathbf{q}_2 \right\| = \sqrt{x_{q_2}^2 + y_{q_2}^2 + 1}$ is the distance between the normalized projection point Q_2 and the camera O_C while considering (3.25). Beware that the newly found location of P_2 is given with respect to the real camera frame, [C].

Again, we obtain the back-projection ray

$$ {}^{[F_2]}\mathbf{v}_2 = {}^{[F_2]}_{[C]}T_2 {}^{[C]}\mathbf{p}_{2,h} \text{ , where } {}^{[F_2]}_{[C]}T_{2_{(3\times4)}} = \Big[\mathbf{I}_{(3)}, \qquad -\mathbf{f}_2 \Big] \tag{3.28} $$

in order to indicate the direction leaving from the primary focus F_2 toward P_w through P_2. Here, the corresponding elevation and azimuth angles are respectively given by

$$ {}^{[F_2]}\theta_2 = \arcsin\left(\frac{z_{\mathbf{v}_2}}{\left\| {}^{[F_2]}\mathbf{v}_2 \right\|} \right) = \arcsin\left(\frac{d - t_2}{\left\| {}^{[F_2]}\mathbf{v}_2 \right\|} \right) \tag{3.29} $$

$$ {}^{[F_2]}\psi_2 = \arctan\left(\frac{y_{\mathbf{v}_2}}{x_{\mathbf{v}_2}} \right) = \arctan\left(\frac{y_2}{x_2} \right) \tag{3.30} $$

where $\| {}^{[F_2]}\mathbf{v}_2 \| = \sqrt{x_2^2 + y_2^2 + (c_2 - t_2)^2}$ is the magnitude of the direction vector from its reflection point P_2.

Like done for the (forward) projection, it is convenient to define the back-projection functions $\mathbf{f}_{\beta_1}$ and $\mathbf{f}_{\beta_2}$ for lifting a 2D pixel point ${}^{[I]}\boldsymbol{m}$ within valid radial bounds equation (3.16) to their angular components ${}^{[F_i]}(\theta_i, \psi_i)$ with respect to their respective foci frame [F_i] (oriented like [C]) as indicated by equations (3.22),(3.23) and (3.29),(3.30), such that $\mathbf{f}_{\beta_i} : \mathbb{R}^2 \mapsto \mathbb{R}^2$, which is implemented as follows:

$$ \mathbf{f}_{\beta_i}({}^{[I]}\boldsymbol{m}) := \begin{cases} \left({}^{[I]}\boldsymbol{m} \xmapsto{(3.22)} {}^{[F_1]}\theta_1, {}^{[I]}\boldsymbol{m} \xmapsto{(3.23)} {}^{[F_1]}\psi_1 \right) & \text{if } i = 1, \\ \left({}^{[I]}\boldsymbol{m} \xmapsto{(3.29)} {}^{[F_2]}\theta_2, {}^{[I]}\boldsymbol{m} \xmapsto{(3.30)} {}^{[F_2]}\psi_2 \right) & \text{if } i = 2, \\ None & \neg(3.16). \end{cases} \tag{3.31} $$

3.3 Field-of-View

The horizontal FOV is clearly 360° for both mirrors. In other words, azimuths ψ can be measured in the interval $[0, 2\pi)$ rad.

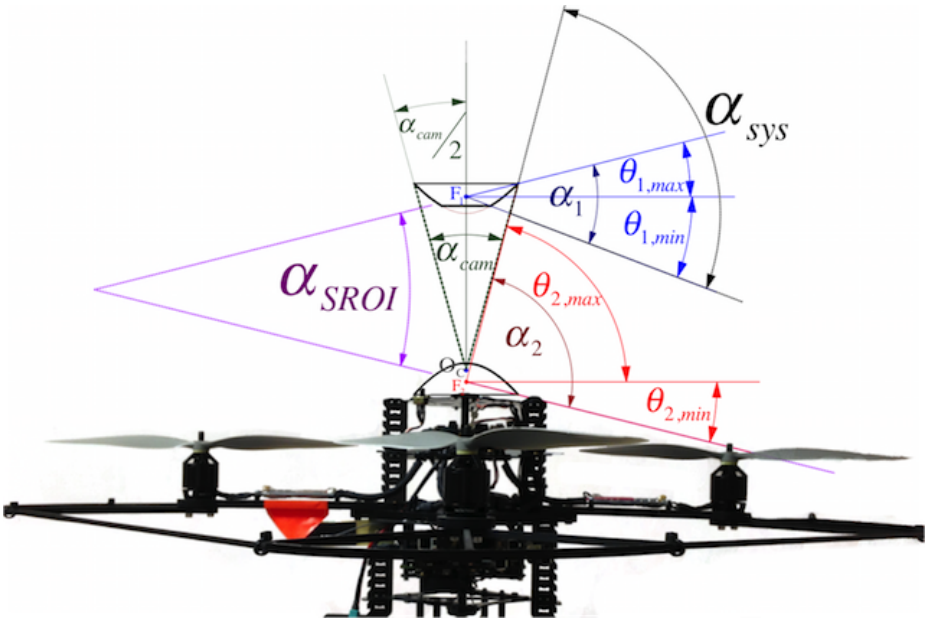

Figure 5: Vertical Field of View (vFOV) angles: α_1 and α_2 are the individual vFOV angles of the mirrors formed by their respective limits $\theta_{1/2,min/max}$; α_{sys} is the overall vFOV angle of the system; and α_{SROI} indicates the angle of the overlapping region conceived from vFOVs α_1 and α_2.

As discussed previously, there exists a positive correlation between the vertical field of view (vFOV) angle α_i of mirror i and its profile parameter k_i, such that $\alpha_i \to 180^\circ$ as $k_i \to \infty$ (see Figure 9). As demonstrated in Figure 5, α_i is physically bounded by its corresponding elevation angles: $\theta_{i,max}$, $\theta_{i,min}$. Both vFOV angles, α_1 and α_2, are computed from their elevation limits as follows:

$$\alpha_1 = \theta_{1,max} - \theta_{1,min} \tag{3.32a}$$

$$\alpha_2 = \theta_{2,max} - \theta_{2,min} \tag{3.32b}$$

In fact, the overall vFOV of the system is also given from these elevation limits:

$$\alpha_{sys} = \max\left(\theta_{1,max}, \theta_{2,max}\right) - \min\left(\theta_{1,min}, \theta_{2,min}\right) \tag{3.33}$$

Figure 6 highlights the the so-called common vFOV angle, α_{SROI}, for the overlapping region of interest (Stereo ROI) where the same point can be seen from both mirrors so stereo computation can be performed (Section 5). In our model, α_{SROI} can be decided from the value of the three prevailing elevation angles ($\theta_{1,max}$, $\theta_{1,min}$, and $\theta_{2,min}$), such that:

$$\alpha_{SROI} = \theta_{SROI,max} - \theta_{SROI,min} \tag{3.34}$$

where generally,

$$\theta_{SROI,min} = \max(\theta_{1,min}, \theta_{2,min}) \tag{3.35a}$$

$$\theta_{SROI,max} = \min(\theta_{1,max}, \theta_{2,max}) \tag{3.35b}$$

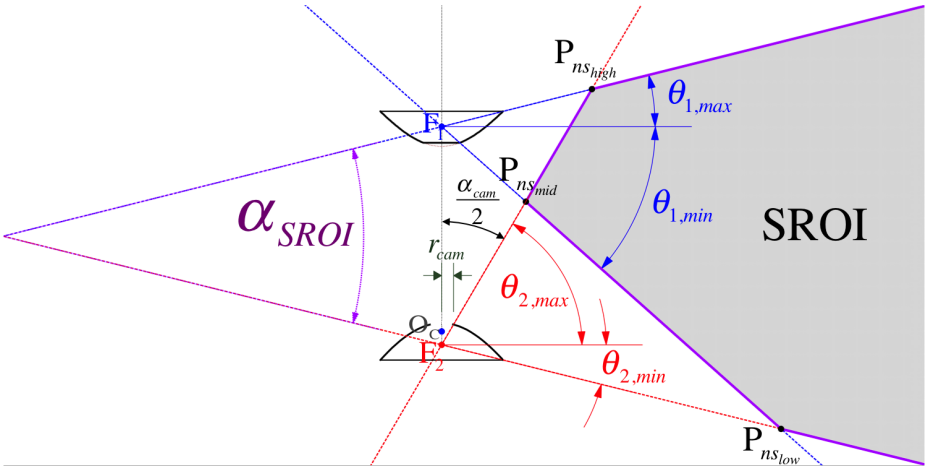

Figure 6: A cross section of the Stereo ROI (shaded area) formed by the intersection of view rays for the limiting elevations $\theta_{1/2,min/max}$. The nearest stereo (ns) points are labeled $\mathrm{P}_{ns_{high}}$, $\mathrm{P}_{ns_{mid}}$ and $\mathrm{P}_{ns_{low}}$ since they are the vertices of the hull that near-bounds the set of usable points for depth computation from triangulation (Section 5.2). See the Table 3 for an example.

The shaded area in Figure 6 illustrates the Stereo ROI that is far-bounded by the set of triangulated points found at the maximum range due to minimum disparity $\Delta m_{12} = 1\,\mathrm{px}$ in the discrete case (refer to Figure 17), such that

$$\begin{aligned} P_{fs} = \{\, \mathrm{P}_w \leftarrow \mathbf{f}_\Delta((\theta_1,\psi_1),(\theta_2,\psi_2)) \,|\, & (\theta_1,\psi_1) \leftarrow \mathbf{f}_{\beta_1}(\boldsymbol{m_1}) \\ & \wedge (\theta_2,\psi_2) \leftarrow \mathbf{f}_{\beta_2}(\boldsymbol{m_2}) \\ & \wedge \Delta m_{12} = 1,\mathrm{px}\} \end{aligned} \tag{3.36}$$

where functions $\mathbf{f}_{\beta_i}$ and $\mathbf{f}_\Delta$, are provided in (3.31) and (5.10).

The Stereo ROI is near-bounded (to the Z-axis of radial symmetry) by its vertices $\mathrm{P}_{ns_{high}}$, $\mathrm{P}_{ns_{mid}}$ and $\mathrm{P}_{ns_{low}}$, which result from the following ray-intersection cases:

a) $\mathrm{P}_{ns_{high}} \leftarrow \mathbf{f}_\Delta((\theta_{1,max},\psi_1),(\theta_{2,max},\psi_2))$

b) $\mathrm{P}_{ns_{mid}} \leftarrow \mathbf{f}_\Delta((\theta_{1,min},\psi_1),(\theta_{2,max},\psi_2))$

c) $\mathrm{P}_{ns_{low}} \leftarrow \mathbf{f}_\Delta((\theta_{1,min},\psi_1),(\theta_{2,min},\psi_2))$

where (again) the intersection function $\mathbf{f}_\Delta$ is implemented for direction rays (or angles) as defined in the Triangulation Section 5.2.

By assuming a radial symmetry on the camera's field of view α_{cam}, it should allow for a complete view of the mirror surface at its outmost diameter of $2r_{1,max} = 2r_{sys}$ according to equation (2.6). Substantially, as depicted in Figure 6, α_{cam} is upper-bounded by the camera hole radius r_{cam} selected

according to equation (4.15). The following inequality constraint emerges

$$2\arctan\left(\frac{r_{sys}}{\mathrm{f}_{z_1}(r_{sys})}\right) \leq \alpha_{cam} \leq 2\arctan\left(\frac{r_{cam}}{\mathrm{f}_{z_2}(r_{cam})}\right) \tag{3.37}$$

where the respective function f_{z_i} is defined in (2.13).

Our specific viewing requirements when mounting the omnidirectional sensor along the central axis of the quadrotor ensure that objects located at 15 cm under the rig's base and at 1 meter away (from the central axis) can be viewed. Thus, angles $\theta_{1,min}$ and $\theta_{2,min}$ should only be large enough as to avoid occlusions from the MAV's propellers (Figure 5) and to produce inner and outer ring images at useful ratio (Figure 7).

3.4 Spatial Resolution

The resolution of the images acquired by our system are not space invariant. In fact, an omnidirectional camera producing spatial resolution-invariant images can only be obtained through a non-analytical function of the mirror profile as shown in [8]. In this section, we study the effect our design has on its spatial resolution as it depends on position parameters like d and c_i introduced in Section 2.1 as well as a direct dependency on the characteristics (e.g. focal length f) of the camera obtaining the image.

Let η_{cam} be the spatial resolution for a conventional perspective camera as defined by Baker and Nayar in [3] and [27]. It measures the ratio between the infinitesimal solid angle $\mathrm{d}\omega_i$ (usually measured in steradians) that is directed toward a point P_i at an angle $\theta_{i,\mathrm{pix}}$ (formed with the optical axis $\mathrm{Z_C}$) and the infinitesimal element of image area $\mathrm{d}A_{\mathrm{pix}}$ that $\mathrm{d}\omega_i$ subtends (as shown in Figure 8). Accordingly, we have:

$$\eta_{cam} = \frac{\mathrm{d}A_{\mathrm{pix}}}{\mathrm{d}\omega_i} = \frac{f^2}{\cos^3\theta_{i,\mathrm{pix}}} \tag{3.38}$$

whose behavior tends to decrease as $\theta_{\mathrm{pix}} \to 0$, so higher resolution areas on the sensor plane continuously increase the farther away they get from the optical center indicated at ${}^{[I]}\boldsymbol{m}_c$. For ease of visualization, we plot only the u pixel coordinates corresponding to the 2D spatial resolution $\eta_{2\mathrm{D}}$, which is obtained by projecting the solid angle Ω onto a planar angle θ_Ω (the apex 2D angle of the solid cone of view). This yields $\theta_\Omega = 2\arccos(1-\Omega/2\pi)$, and we reduce the image area into its circular diameter with $2\sqrt{\mathrm{d}A/\pi}$. Generally, our conversion from 3D spatial resolution η in $\left[\mathrm{m}^2/\mathrm{sr}\right]$ units to 2D proceeds as follows:

$$\eta_{2\mathrm{D}} = \frac{2\sqrt{\eta/\pi}}{\theta_{\Omega=1\,\mathrm{sr}}} \tag{3.39}$$

where $\theta_{\Omega=1\,\mathrm{sr}} \approx 1.14390752211\,\mathrm{rad}$.

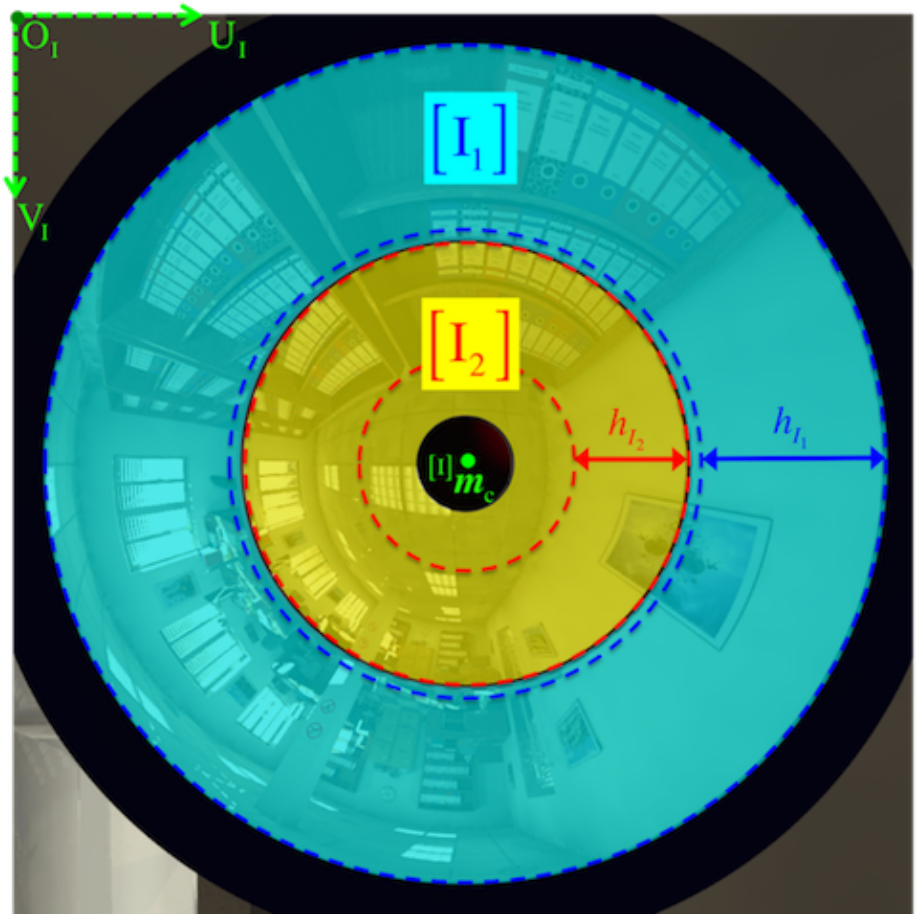

Figure 7: The omnidirectional image [I] shown in Figure 2b is now annotated for the separate regions of interest in $[I_1]$ and $[I_2]$ from the corresponding projections onto their image planes π_{img_i}. In addition, we indicate the corresponding radial heights h_{I_1} and h_{I_2} for the Stereo ROI that are used determine the imaging ratio $\chi_{I_{1:2}} = \frac{h_{I_1}}{h_{I_2}}$.

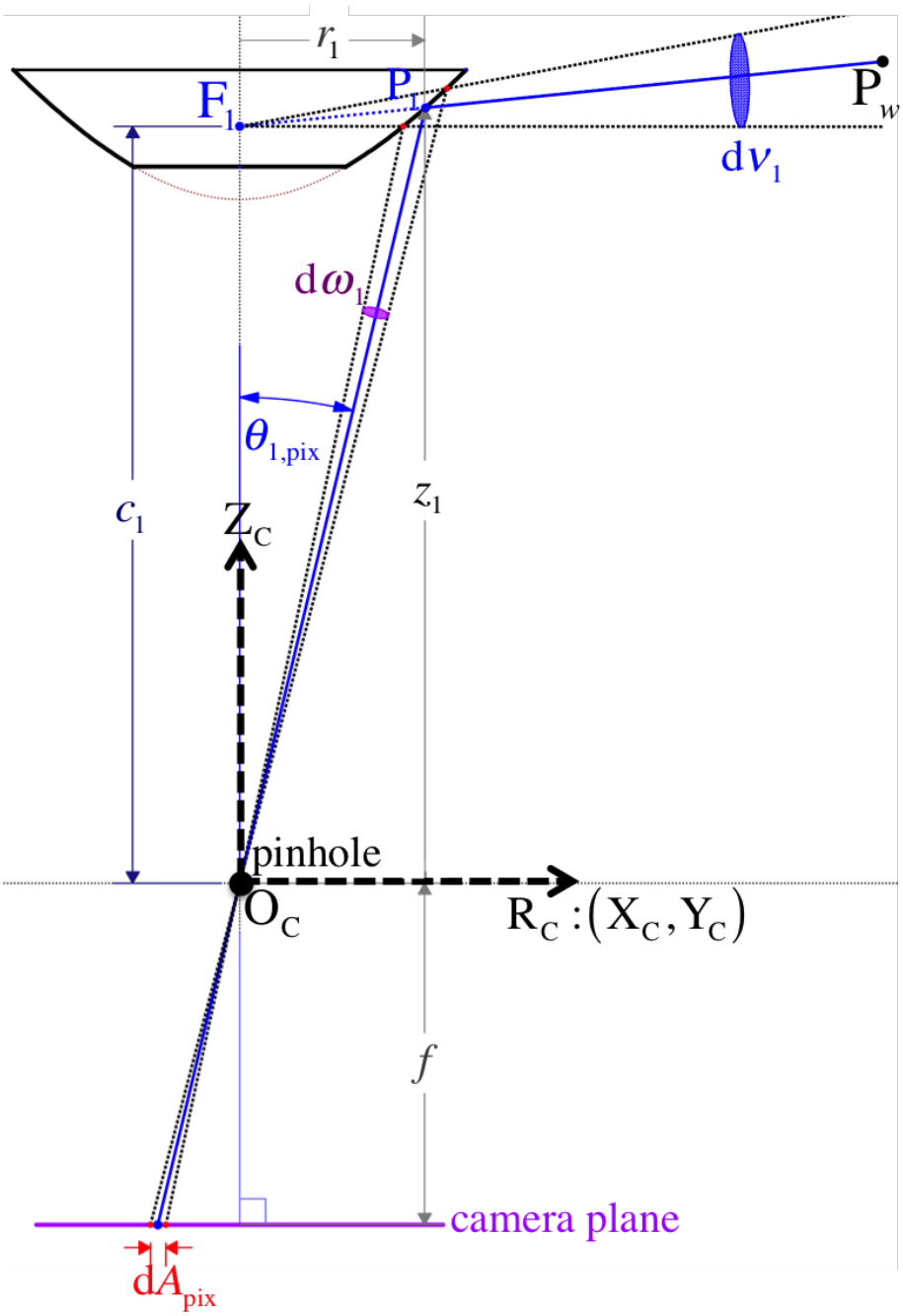

Figure 8: The spatial resolution for the central catadioptric sensor is the ratio between a infinitesimal element of image area dA and the corresponding solid angle infinitesimal element dν_1 that views the world point P_w. (Notice that only mirror 1 is drawn in 2D and infinitesimal elements are exaggerated for easier visualization.)

More specifically, equation (3.38) is manipulated to provide $\eta_{i,cam}$ as the indicative of spatial resolution toward any specific point in the mirror, ${}^{[\mathrm{C}]}\mathrm{P}_i \in M_i$ according to equation (2.8), as follows:

$$\eta_{i,cam} = \begin{cases} f^2 \left(\frac{\sqrt{r_1^2+z_1^2}}{z_1} \right)^3 & \text{if } i = 1, \\ f^2 \left(\frac{\sqrt{r_2^2+(d-z_2)^2}}{d-z_2} \right)^3 & \text{if } i = 2. \end{cases} \tag{3.40}$$

where r_i is the radial length defined in equation (2.6) and its associated z_i coordinate, f is the camera's focal length, and the design parameters d and c_i that relate to the position of the mirror focal points F_i with respect to the camera frame [C].

Thus, for a conventional perspective camera, $\eta_{i,cam}$ grows as $\theta_{i,\mathrm{pix}} \to \pi/2$ due to the foreshortening effect that stretches the image representation around the sensor plane's periphery that collects spatial information onto a larger number of pixels. Therefore, image areas farther from the optical axis are considered to have higher spatial resolutions.

Baker and Nayar also defined the resolution, η_i, of a catadioptric sensor in order to quantify the view of the world or $\mathrm{d}\nu_i$, an infinitesimal element of the solid angle subtended by the mirror's effective viewpoint F_i, which is consequently imaged onto a pixel area $\mathrm{d}A_{\mathrm{pix}}$. Again, here we provide the resolution according to our model:

$$\eta_1 = \frac{\mathrm{d}A_{\mathrm{pix}}}{\mathrm{d}\nu_1} = \left[\frac{r_1^2 + (c_1 - z_1)^2)}{r_1^2 + z_1^2} \right] \eta_{1,cam} \tag{3.41a}$$

$$\eta_2 = \frac{\mathrm{d}A_{\mathrm{pix}}}{\mathrm{d}\nu_2} = \left[\frac{r_2^2 + (c_2 - d + z_2)^2)}{r_2^2 + (d - z_2)^2} \right] \eta_{2,cam} \tag{3.41b}$$

for our mirror-perspective camera configuration, where O_C is the origin of coordinates as shown in Figure 8 and $\eta_{i,cam}$ is given in equation (3.40).

As demonstrated by the plot of Figure 12 in Section 4.2.1, η_i grows accordingly towards the periphery of each mirror (the equatorial region). This aspect of our sensor design is very important because it indicates that the common field of view, α_{SROI}, where stereo vision is employed (Section 5), is imaged at relatively higher resolution than the unused polar regions closer to the optical axis (the Z_C axis).

If we modify η_i by substituting r_i with its equivalent $\mathrm{f}_{r_i}(z_i)$ function defined in (2.14), using mirror 1 for example, we get:

$$\begin{aligned} \eta_1 &= \left[\frac{\mathrm{f}_{r_1}^2(z_1) + (c_1 - z_1)^2}{\mathrm{f}_{r_1}^2(z_1) + z_1^2} \right] \eta_{1,cam} \\ &= \frac{f^2 \sqrt{\mathrm{f}_{r_1}^2(z_1) + z_1^2} \left[\mathrm{f}_{r_1}^2(z_1) + (c_1 - z_1)^2 \right]}{z_1^3} \end{aligned} \tag{3.42}$$

which is an inherent indicative of how the resolution η_i for a reflection point P_i increases with $k \to \infty$, as plotted in Figure 11. Conversely, the smaller the k_i parameter gets (as it relates to eccentricity, see

Section 2.2), the flatter the mirror becomes, so its resolution resembles more that of the perspective camera alone, or mathematically $\lim_{k_i \to 2} \eta_i \to \eta_{i,cam}$.

As shown in Figure 9, a smaller k_i would require a wider radius r_{sys} in order to achieve the same omnidirectional vertical field of view, α_{sys}. Even worse, in order to image such a wider reflector, either the camera's field of view, α_{cam}, would have to increase (by decreasing the focal length f and perhaps requiring a larger camera hole r_{cam} and sensor size), or the distance c_i between the effective pinhole and the viewpoint would have to increase accordingly. Another consequence, it is the effect on the baseline b, which must change in order to maintain the same vertical field of views (Figure 10). As a result, the depth resolution of the stereo system would suffer as indicated next.

4 Parameter Optimization and Prototyping

The nonlinear nature of this system makes it very difficult to balance among its desirable performance aspects. The optimal vector of design parameters, $\boldsymbol{\theta}^*$, can be found by posing a constrained maximization problem for the objective function

$$\mathrm{f}_b(\boldsymbol{\theta}) = c_1 + c_2 - d \tag{4.1}$$

which measures the baseline according to equation (2.3). Indeed, the optimization problem is subject to the set of constraints C, which we enumerate in Section 4.1. Formally,

$$\boldsymbol{\theta}^* = \arg\max_{\boldsymbol{\theta} \in \Theta} \mathrm{f}_b(\boldsymbol{\theta}) \;\; \text{subject to } C \tag{4.2}$$

where $\Theta \subseteq \mathbb{R}^6$ is the 6-dimensional solution space for $\boldsymbol{\theta} \in \mathbb{R}^6$ given in (2.4) as $\boldsymbol{\theta} = \begin{bmatrix} c_1, & c_2, & k_1, & k_2, & d, & r_{sys} \end{bmatrix}$.

4.1 Optimization Constraints

This section discusses the constraints that the proposed omnistereo sensor is subject to. Overall, we mainly take the following into account:

a) *geometrical constraints*, including SVP and reflex constraint, as described by equations (2.11), (2.12), and (2.2);

b) *physical constraints*, these are the rig's dimensions, which include the mirrors radii as well as by-product parameters such as system height h_{sys} and mass m_{sys};

c) *performance constraints*, where the spatial resolution and range from triangulation are determined by parameters k_1, k_2, and c_1, and the desired viewing angles for an optimal Stereo ROI and the related common field of view, α_{SROI}.

Following the design model described throughout Section 2, we now list the pertaining linear and nonlinear constraints that make the set C. We disjoint the linear constraints in a subset C_L so

those non-linear constraints belong to another subset C_{NL}, and $C = C_L \uplus C_{NL}$. Within each subset, we generalize equality constraints as functions $\mathrm{h}\colon \mathbb{R}^6 \mapsto \mathbb{R}$ that obey

$$\mathrm{h}(\boldsymbol{\theta}) = 0 \tag{4.3}$$

whereas inequality functions $\mathrm{g}\colon \mathbb{R}^6 \mapsto \mathbb{R}$ satisfy

$$\mathrm{g}(\boldsymbol{\theta}) \leq 0 \tag{4.4}$$

4.1.1 Linear Constraints

We have only setup linear inequalities for constraints in C_L. Specifically, we require the following:

g_1: The focal distance c_2 of mirror 2 must be longer than d (distance between $\mathrm{O_C}$ and F_{2v}). Requiring that

$$d \leq c2 \tag{4.5}$$

in order to set the position of F_2 below the origin $\mathrm{O_C}$ of the pinhole camera frame [C].

g_2: Mirror 1's focal separation, c_1, needs to exceed the placement of the reflex mirror. By letting

$$d/2 \leq c_1 \tag{4.6}$$

the hyperboloidal mirror can reflect light towards its effective viewpoint F_1 without being occluded by the reflex mirror.

g_3: The empirical constraint

$$\frac{5}{3} \leq \frac{k_2}{k_1} \tag{4.7}$$

pertains our rig dimensions in order to assign a greater curvature to mirror 2's profile (located a the bottom), so it can look more toward the equatorial region rather than up. Complementarily, this constraint flattens mirror 1's profile, so it can possess a greater view of the ground rather than the sky. This curvature inequality allows the Stereo ROI to be bounded by a wider vertical field of view when the sensor must be mounted above the MAV propellers as depicted in Figure 5.

4.1.2 Non-Linear Constraints

For the non-linear design constraints, we have the following inequalities:

g_4: The AscTec Pelican quadrotor has a maximum payload of 650 g (according to the manufacturer specifications [28]). Therefore, we must satisfy the system mass' equation computed via (2.16), such that

$$m_{sys} \leq 650 \tag{4.8}$$

g_5: Similarly, we limit the system's height equation (2.15) by $h_{sys,max}$.

$$h_{sys} \leq h_{sys,max} \tag{4.9}$$

For example, we set $h_{sys,max} = 150\,\text{mm}$ for the 37 mm-radius rig.

g_6: The origin of coordinates for the camera frame is set at it viewpoint, O_C. In order to fit the camera enclosure under mirror 2, it is realistic to position the vertex on the vertical transverse axis at more than 5 mm away from O_C:

$$5 \leq z_{0_2} - a_2 \tag{4.10}$$

where z_{0_2} is defined in (2.10), and a_2 pertains to (2.5).

Next, we determine the bounds for the limiting angles that partake in the computation of the system's vertical field of view α_{sys}, which is based on equation (3.33). Our application has specific viewing requirements that can be achieved with the following conditions:

g_7: Let $\Lambda_{1,max} = 14^\circ$ be an acceptable upper-bound for angle $\theta_{1,max}$, such that:

$$\theta_{1,max} \leq \Lambda_{1,max} \tag{4.11}$$

g_8: Because we desire a larger view towards the ground from mirror 1, we empirically set $\Lambda_{1,min} = -25^\circ$ as a lower-bound for the minimum elevation $\theta_{1,min}$:

$$\Lambda_{1,min} \leq \theta_{1,min} \tag{4.12}$$

g_9: In order to avoid occlusions with the MAV's propellers while being capable to image objects located about 5 cm under the rig's base and 20 cm away from the central axis, we limit mirror 2's lowest angle by a lower-bound $\Lambda_{2,min} = -14^\circ$. Symbolically,

$$\Lambda_{2,min} \leq \theta_{2,min} \tag{4.13}$$

Finally, we restrict the radius of the system, r_{sys}, to be identical for both hypeboloids by satisfying the following equality condition:

h_1: With functions f_{r_1} and f_{r_2} defined in (2.14), we set

$$r_{sys} = r_{i,max} = f_{r_i}(z_{i,max}), \forall i \in \{1,2\}$$

where we imply that $z_{i,max} \leftarrow f_{z_i}(r_{sys})$ using equation (2.13). Thus, the entire function composition for this equality becomes

$$f_{r_1}\left(f_{z_1}(r_{sys})\right) = f_{r_2}\left(f_{z_2}(r_{sys})\right) \tag{4.14}$$

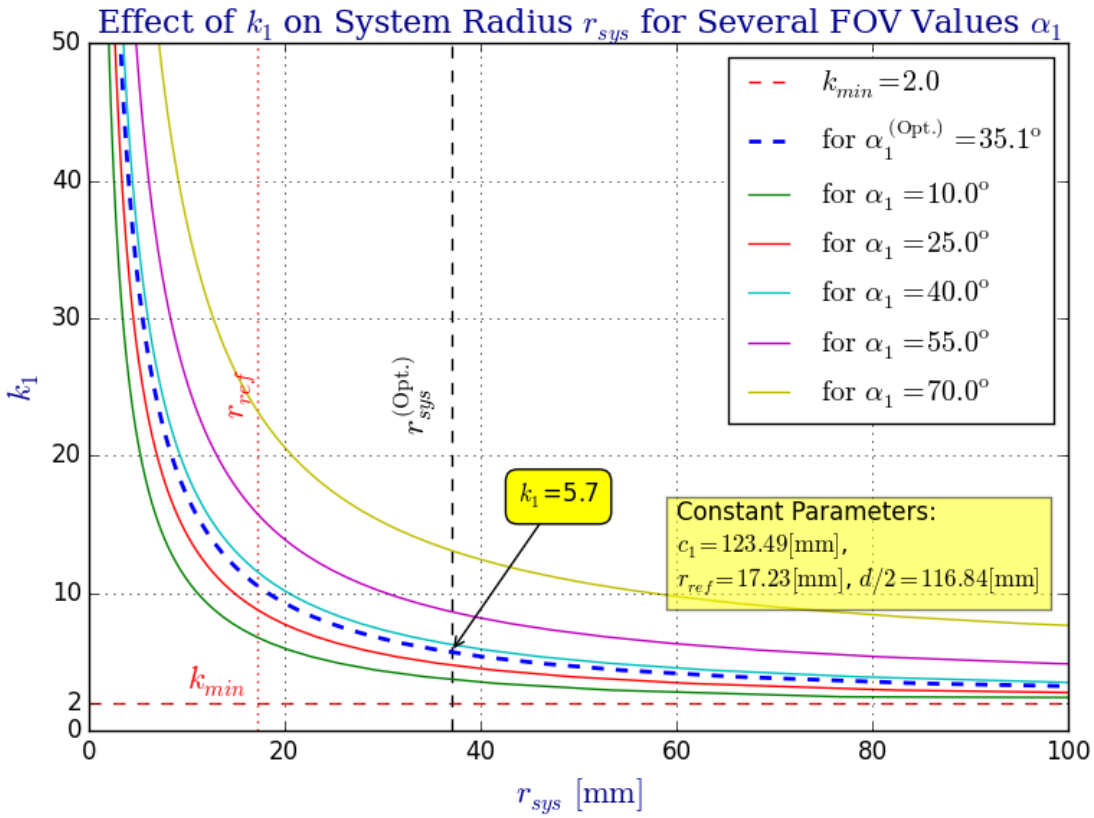

Figure 9: The effect that parameter k_i (showing mirror 1 only) has over the system radius r_{sys} for various vertical field of view angles α_1. In order to maintain a vertical field of view α_i that is bounded by $z_{max}|_{r_{sys}}$, the value of r_{sys} must change accordingly. Inherently, the system's height, h_{sys}, and its mass, m_{sys}, are also affected by k_i (see Section 2.3).

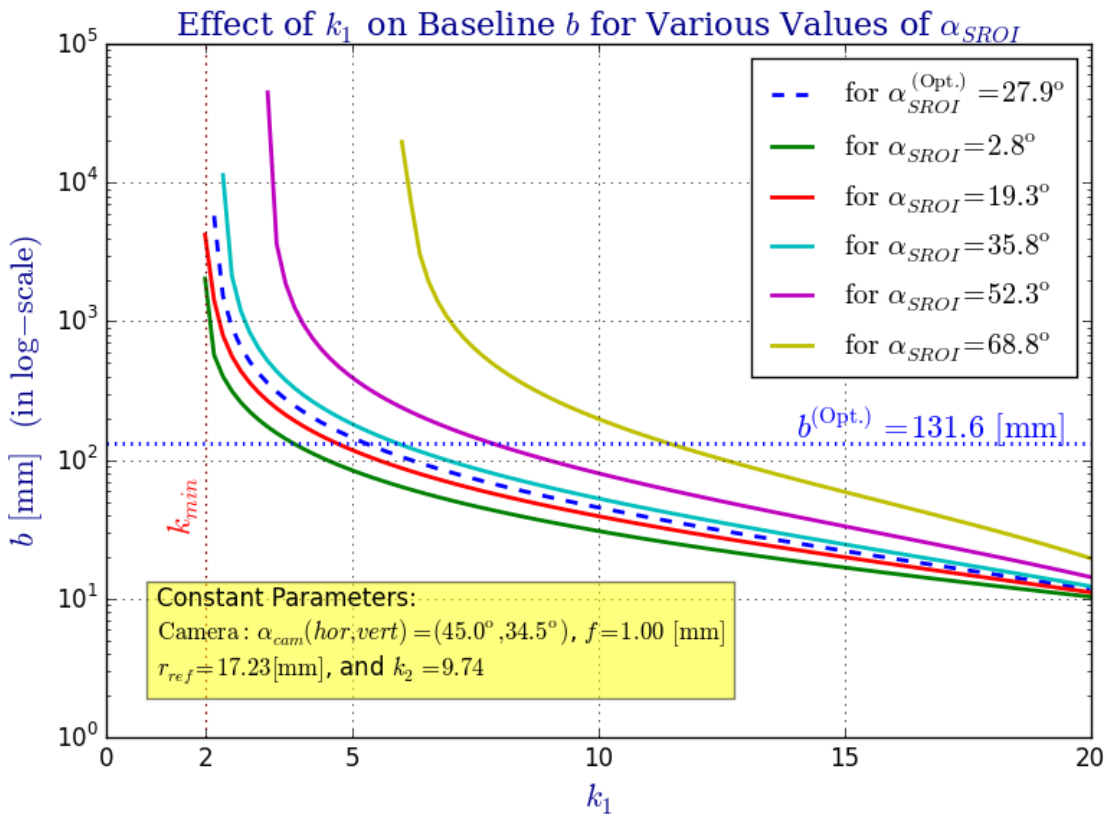

Figure 10: The effect that parameter k_1 has over the omnistereo system's baseline b for several common FOV angles (α_{SROI}) and a fixed camera with α_{cam}. An inverse relationship exists between k and b as plotted here (using a logarithmic scale for the vertical axis). Intuitively, the flatter the mirror gets ($k \to 2$), the farther F_1 must be translated in order to fit within the camera's view, α_{SROI}, causing b to increase.

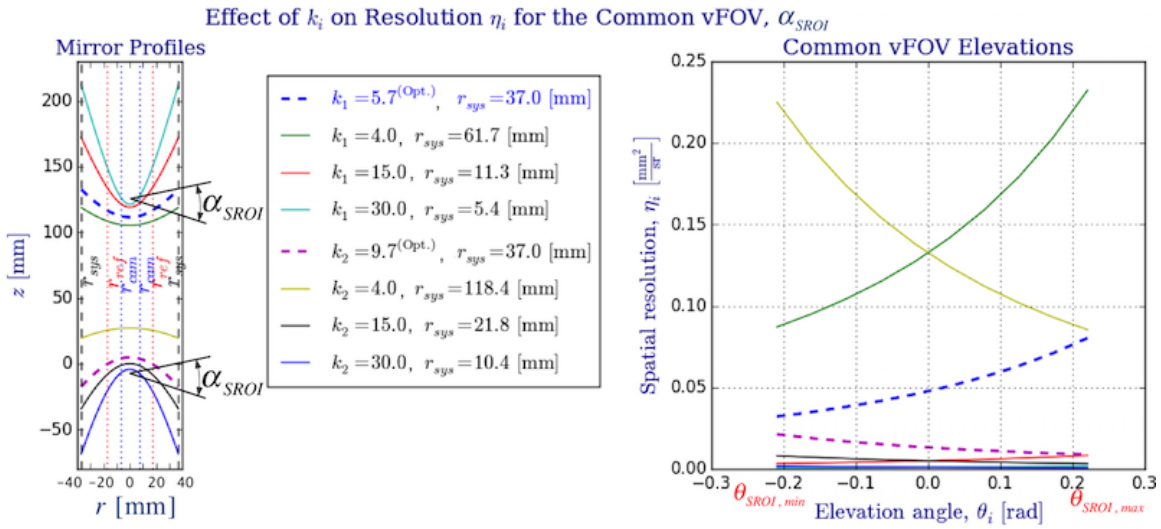
Effect of k_i on Resolution η_i for the Common vFOV, α_{SROI}
Mirror Profiles
Common vFOV Elevations
$k_1 = 5.7^{(Opt.)}$, $r_{sys} = 37.0$ [mm]
$k_1 = 4.0$, $r_{sys} = 61.7$ [mm]
$k_1 = 15.0$, $r_{sys} = 11.3$ [mm]
$k_1 = 30.0$, $r_{sys} = 5.4$ [mm]
$k_2 = 9.7^{(Opt.)}$, $r_{sys} = 37.0$ [mm]
$k_2 = 4.0$, $r_{sys} = 118.4$ [mm]
$k_2 = 15.0$, $r_{sys} = 21.8$ [mm]
$k_2 = 30.0$, $r_{sys} = 10.4$ [mm]
α_{SROI}
α_{SROI}
z [mm]
r [mm]
Spatial resolution, η_i $\left[\frac{\text{mm}^2}{\text{sr}}\right]$
Elevation angle, θ_i [rad]
$\theta_{SROI,min}$
$\theta_{SROI,max}$

Figure 11: Comparison of k_i values and their effect on spatial resolution η_i. Note that for the big rig, the optimal focal dimensions c_1 and c_2 (from Table 1) were used as well as the angular span on the common vertical FOV, $\alpha_{SROI} \approx 28°$. Although resolution $\eta_i^{(Opt.)}$ for the optimal values of k_i could be improved by employing smaller k values (lower curvature profiles indicated on the left plot of the figure), these would in turn increase the system radius, r_{sys}, so they are not desirable. As expected, we appreciate how the spatial resolutions, η_i for $i = \{1,2\}$, increase towards the equatorial regions ($\theta_1 \rightarrow \theta_{SROI,max}$ and $\theta_2 \rightarrow \theta_{SROI,min}$).

Table 2: By-product Length Parameters

Parameter	Big Rig	Small Rig
r_{ref}[mm]	17.23	11.74
r_{cam}[mm]	7	7
h_{sys}[mm]	150.00	120.00

4.2 Optimal Results

Applying the aforementioned constraints (Section 4.1) and using an iterative nonlinear optimization method such as one of the surveyed in [7], a bounded solution vector $\boldsymbol{\theta}^*$ converges to the following values for two rig sizes:

Table 1: Optimal System Design Parameters

Parameter	Big Rig	Small Rig
$b = \max \mathrm{f}_b(\boldsymbol{\theta}^*)$	131.61	108.92
r_{sys}[mm]	37.0	28.0
c_1[mm]	123.49	104.59
c_2[mm]	241.80	204.34
d[mm]	233.68	200.00
k_1	5.73	6.88
k_2	9.74	11.47

As Figure 3 illustrates, a realistic dimension for the radius of the camera hole, r_{cam}, must consider the maximum value between a physical micro-lens radius (r_{lens}) and the radius $r_{\alpha_{cam}}$ for an unoccluded field of view of the camera (α_{cam}). Practically,

$$r_{cam} = \max\left(r_{lens}, r_{\alpha_{cam}}\right) \tag{4.15}$$

Table 2 contains the derived dimensions corresponding to the parameters listed in Table 1.

For both rigs, the expected vertical field of views are $\alpha_{sys} = 75^\circ - (-21^\circ) \approx 96^\circ$ according to equation (3.33), and $\alpha_{SROI} = 14^\circ - (-14^\circ) \approx 28^\circ$ using equation (3.34). Note that $\theta_{2,max}$ may be actually limited by the camera hole radius, which in turn reduces $\theta_{cam} \rightsquigarrow 59^\circ$, and the real $\alpha_{sys} \rightsquigarrow 80^\circ$. For the big rig, Table 3 shows the nearest vertices of the Stereo ROI that result from these angles (Figure 6).

Finally, we study the effect parameter k_i has over the system radius r_{sys} (Figure 9), the omnistereo baseline b (Figure 10), and the spatial resolution (Figure 12 and Figure 11). Figure 9 addresses the relation between k_i and radius r_{sys} (recall the rig size discussion from Section 2.3). It can be seen that for the same r_{sys}, realistic k_1 values fall in the range $3 < k_1 < 13$, whereas the vertical field of

Table 3: Near Vertices of the Stereo ROI for the Big Rig

Vertex	${}^{[C]}\rho_w$ [mm]	${}^{[C]}z_w$ [mm]
$P_{ns_{high}}$	93.5	144.4
$P_{ns_{mid}}$	65.2	98.4
$P_{ns_{low}}$	763.4	−170.3

view $\alpha_1 \to 0$ as $k \to 2$ as expected according to the SVP property specified in Section 2.2. In fact, the left part of Figure 11 also demonstrates the necessary r_{sys} to maintain $\alpha_{SROI} \approx 28^\circ$ for various values of k_i.

Figure 10 shows the inverse relationship between values of k_1 and the baseline, b, as we attempt to fit the view of a wider/narrower mirror profile (due to k_1) on the constant camera field of view (α_{cam}). In order to make a fair comparison, let

$$k_1' = k_1 + \varepsilon_k, \quad \forall k_1 > 2, \varepsilon_k > 0$$

for which we find its new focal length c_1' while solving for the new r_{sys}' and z_{max}'. Provided with a function such that $c_1 \leftarrow \mathrm{f}_{c_1}(k_1)$, we perform the analysis for a given α_{SROI} and α_{cam} shown in Figure 10. Given the baseline function f_b defined in (4.1), the following implication holds true:

$$\mathrm{f}_b\,|_{c_1 \leftarrow \mathrm{f}_{c_1}(k_1)} > \mathrm{f}_b\,|_{c_1' \leftarrow \mathrm{f}_{c_1}(k_1+\varepsilon_k)},\ \forall k_1 > 2, \varepsilon_k > 0 \tag{4.16}$$

Notice that k_2, c_2 and d are kept constant through this analysis, and we ignore possible occlusions from the reflex mirror located at $d/2$.

4.2.1 Spatial Resolution Optimality

In this section, we compare the sensor's spatial resolution, η_i, defined in Section 3.4 for the optimal parameters listed in Table 1 (for the big rig, only). In Figure 12, we verify how both resolutions η_1 and η_2 increase towards the equatorial region according to the spatial resolution theory presented in [3]. Indeed, the increase in spatial resolution within the Stereo ROI that covers the equatorial region (as indicated in Figure 6) justifies our model's coaxial configuration intended as an omnistereo application.

In Figure 11, we compare the effect on η_i for various mirror profiles, which depend directly on k_i. We illustrate the change in curvature due to parameter k_1 and k_2 and also show (in the legend) the respective r_{sys} achieving a common vFOV, $\alpha_{SROI} \approx 28^\circ$ as for the optimal parameter of the big rig. From this plot, we appreciate the compromise due to optimal parameters, $k_1^{(Opt.)} = 5.7$ and $k_2^{(Opt.)} = 9.7$, for a balanced system size due to r_{sys} and a suitable range of spatial resolutions, η_i, within the Stereo ROI enveloped by α_{SROI}.

For the optimal parameter values listed in Table 1, we find that $\chi_{\mathrm{I}_{1:2}} \approx 2$.

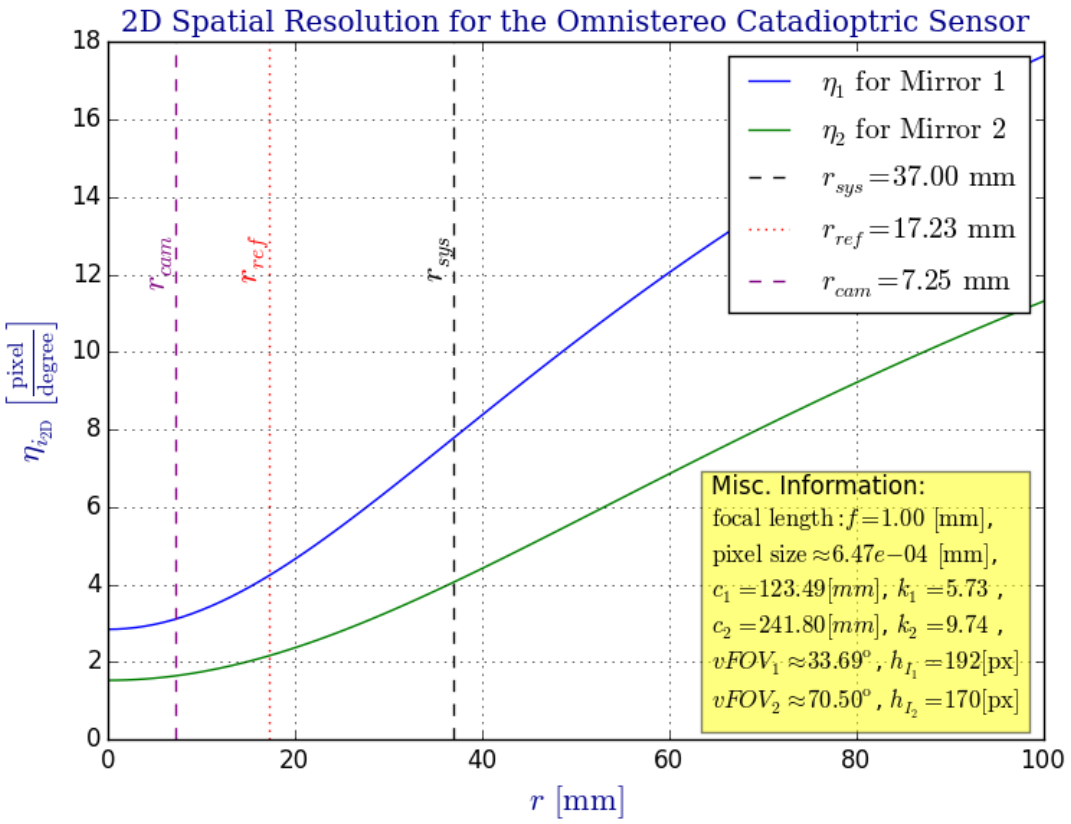

Figure 12: Using the formula given in (3.39), we plot the 2D version of the spatial resolution of our proposed omnistereo catadioptric sensor (37 mm-radius rig). We observe how both resolutions η_1 and η_2 increase towards the equatorial region where they are physically limited by r_{sys}. In turn, this verifies the spatial resolution theory given in [3], and it justifies our coaxial configuration useful for omnistereo within the Stereo ROI indicated in Figure 6.

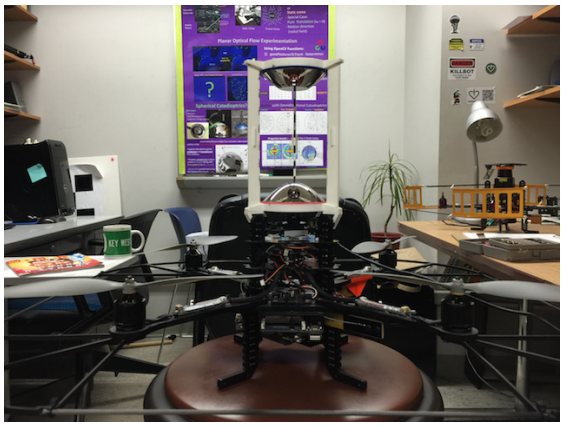

(a) Omnistereo rig using 37 mm-radius mirrors mounted on an AscTec Pelican quadrotor.

(b) Omnidirectional image captured by the real-life prototype in Figure 13a.

Figure 13: Real-life prototypes of the omnistereo sensor. rig.

4.3 Prototypes

We validate our design with both synthetic and real-life models.

4.3.1 Synthetic Prototype (Simulation)

After converging to an optimal solution $\mathrm{f}_b(\boldsymbol{\theta}^*)$, we employ these parameters (Table 1) to describe synthetic models using POV-Ray, an open-source ray-tracer. We render 3D scenes via the simulated omnistereo sensor such as the examples shown in Figure 2. The simulation stage plays two important roles in our investigation:

1) to acquire ground-truth 3D-scene information in order to evaluate the computed range by the omnistereo system (as explained in Section 5, and

2) to provide an almost accurate geometrical representation of the model by discounting some real-life computer vision artifacts such as assembly misalignments, glare from the support tube (motivates use of standoffs on real prototype), as well as the shallow camera's depth-of-field. All of these can affect the quality of the real-life results shown in this manuscript (Section 6.1).

4.3.2 Real-life Prototypes

We have also produced two physical prototypes that can be installed on the Pelican quadrotor (made by Ascending Technologies). A small rig assembled with hyperboloidal mirrors of $r_{sys} \approx 28\,\mathrm{mm}$ (according to the specifications from Table 1).

Figure 13a shows the larger rig constructed with hyperboloidal mirrors of $r_{sys} \approx 37\,\mathrm{mm}$, and a Logitech® HD Pro Webcam C910 camera (2592x1944 pixels at $15 \sim 20$ FPS). We decided to skip the use of acrylic glass tubes to separate the mirrors at the specified h_{sys} distance, and instead we

constructed a thin 3-standoff mount in order to avoid glare and cross-reflections. This support was designed in 3D-CAD and printed for assembly. The three areas of occlusion due to the 3 mm-wide standoffs are considered minimal. In fact, we stamped fiducial markers to the vertical standoffs to aid with the panoramas generation (Section 5.1) and auto-calibration in the future. To image the entire surface of mirror 1, we require a camera with a (minimum) field of view of $\alpha_{cam} > 31^\circ$, which is achieved by $r_{\alpha_{cam}} > 1.4\,\text{mm}$. In practice, as noted by equation (4.15), microlenses measure around $r_{lens} \approx 7\,\text{mm}$. Therefore, we set $r_{cam} > 7\,\text{mm}$, as a safe specification to fit a standard microlens through the opening of mirror 2 as shown in Figure 3.

Recall that m_{sys} is limited by the maximum 650 g-payload that the AscTec Pelican quadrotor is capable of flying with (according to the manufacturer specifications [28]). The camera with lens weights approximately 25 g. The cylindrical tube material is acrylic with average density $\rho_{tub} \approx 1.18\,\text{g}\,\text{cm}^{-3}$, whereas the brass that is used to mold the mirrors has a density $\rho_{mir} \approx 8.5\,\text{g}\,\text{cm}^{-3}$. Empirically, we obtain a close estimate of the entire system's mass, such that $m_{sys} \approx 550\,\text{g}$ for the big rig, and $m_{sys} \approx 150\,\text{g}$ for the small rig.

5 3D Sensing from Omnistereo Images

Stereo vision from point correspondences on images at distinct locations is a popular method for obtaining 3D range information via triangulation. Techniques for image point matching are generally divided between dense (area-based scanning [7]) and sparse (feature description [29]) approaches. Due to parallax, the disparity in point positions for objects close to the vision system is larger than for objects that are farther away. As illustrated in Figure 6, the nearsightedness of the sensor is determined mainly by the common observable space (a.k.a. Stereo ROI) acquired by the limiting elevation angles of the mirrors (Section 3.3). In addition, we will see next (Section 5.2) that the baseline b also plays a major role in range computation.

Due to our model's coaxial configuration, we could scan for pixel correspondences radially between a given pair of warped images $([\text{I}_1], [\text{I}_2])$ like in the approach taken by similar works such as [24]. However, it seems more convenient to work on a rectified image space, such as with panoramic images, where the search for correspondences can be performed using any of the various existing methods for perspective stereo views. Hence, we first demonstrate how these rectified panoramic images are produced (Section 5.1) and used for establishing point correspondences. Then, we proceed to study our triangulation method for the range computation from given set of point correspondences (Section 5.2). Last, we show preliminary 3D point clouds as the outcome from such procedure.

5.1 Panoramic Images

Figure 14 illustrates how we form the respective panoramic image $[\Xi_1]$ out of its warped omnidirectional image $[\text{I}_1]$. As illustrated in Figure 7, $[\text{I}_i]$ is simply the region of interest out of the full image $[\text{I}]$ where projection occurs via mirror i. However, we can safely refer to $[\text{I}]$ because it will never be the case that projections via different mirrors overlap on the same pixel position ${}^{[\text{I}]}\boldsymbol{m}$. In a few words, we obtain a panorama $[\Xi_\text{i}]$ by reverse-mapping each discretized 3D point $\text{P}_{cyl_i} \in S_{cyl_i}$ to its projected

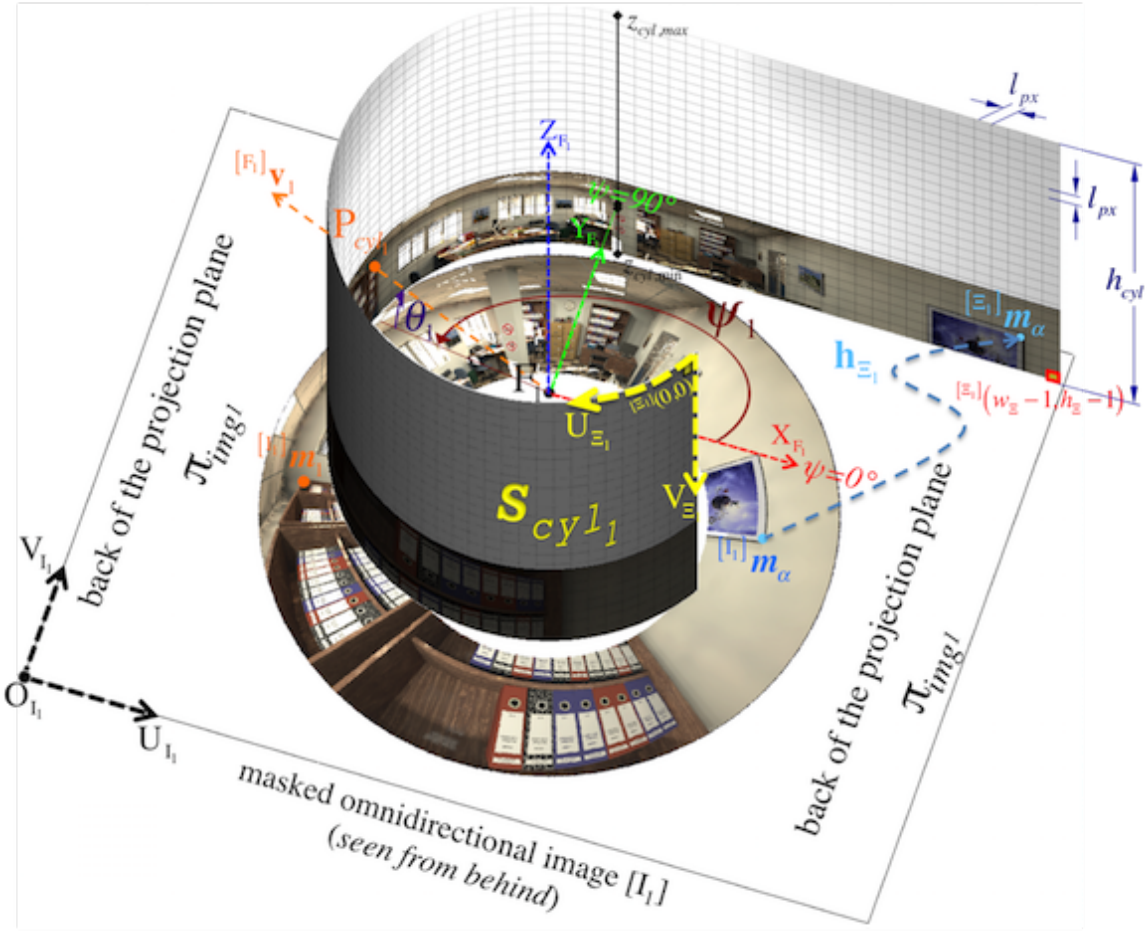

Figure 14: An example for the formation of panoramic image $[\Xi_1]$ out of the omnidirectional image $[\mathrm{I}_1]$ (showing only the masked region of interest on the back of image plane π_{img_1}). Any particular ray, $\mathbf{v}_1$ indicated by its elevation and azimuth such as ${}^{[\mathrm{F}_1]}(\psi_1, \theta_1)$ that is directed towards the focus F_1 must traverse the projection cylinder S_{cyl_1} at point P_{cyl_1}. More abstractly, the figure also shows how a pixel position ${}^{[\Xi_1]}\boldsymbol{m}_\alpha$ on the panoramic pixel space is mapped from its corresponding pixel position ${}^{[\mathrm{I}_1]}\boldsymbol{m}_\alpha$ via function $\mathbf{h}_{\Xi_1}$ defined in (5.6). Although not up to scale, it's crucial to notice the relative orientation between S_{cyl_1} and the *back* of the projection plane π_{img_1} where the omnidirectional image $[\mathrm{I}_1]$ is found.

pixel coordinates ${}^{[\mathrm{I}]}\boldsymbol{m}$ on [I] according to Section 3.2.

More thoroughly, for $i = \{1,2\}$, S_{cyl_i} is the set of all valid 3D points P_{cyl_i} that lie on an imaginary unit cylinder centered along the Z-axis and positioned with respect to the mirror's primary focus F_i. Recall that the radius of a unit cylinder is $r_{cyl} = 1$, so its circumference becomes $w_{cyl} = 2\pi r_{cyl} = 2\pi$. Noticed that the imaging ratio, $\chi_{\mathrm{I}_{1:2}} = \frac{h_{I_1}}{h_{I_2}}$, illustrated in Figure 7 provides a way of inferring the scale between pairs of point correspondences. However, we achieve conforming scales among both panoramic representations by simply setting both cylinders to an equal height h_{cyl}, which is determined from the system's elevation limits, $(\theta_{sys,min}, \theta_{sys,max})$, since they partake in the measurement of the system's vertical field of view (3.33). Therefore, we obtain

$$h_{cyl} = z_{cyl,max} - z_{cyl,min} \text{ , where } \begin{cases} z_{cyl,max} &= \tan\left(\theta_{sys,max}\right) \\ z_{cyl,min} &= \tan\left(\theta_{sys,min}\right) \end{cases} \tag{5.1}$$

Consequently, to achieve panoramic images $[\Xi_\mathrm{i}]$ of the same dimensions by maintaining a true aspect ratio $w_\Xi : h_\Xi$, it suffices to indicate either the width (number of columns) w_Ξ or the height (number of rows) h_Ξ as number of pixels. Here, we propose a custom method for resolving the panoramic image dimensions by setting the equality for the length l_{px} of an individual "square" pixel in the cylinder (behaving like a panoramic camera sensor):

$$l_{px} = \frac{w_{cyl}}{w_\Xi} = \frac{h_{cyl}}{h_\Xi} \tag{5.2}$$

If the width w_Ξ is given, then the height is given by $h_\Xi = w_\Xi h_{cyl}/w_{cyl}$. Otherwise, if h_Ξ is given a priori, we can find $w_\Xi = h_\Xi w_{cyl}/h_{cyl}$.

To increase the processing speed for each panoramic image $[\Xi_\mathrm{i}]$, we fill up its corresponding look-up-table LUT_{Ξ_i} of size $w_\Xi \times h_\Xi$ that encodes the mapping for each panoramic pixel coordinates ${}^{[\Xi_\mathrm{i}]}\boldsymbol{m} = {}^{[\Xi_\mathrm{i}]}\begin{bmatrix} u, & v \end{bmatrix}^\mathsf{T}$ to its respective projection ${}^{[\mathrm{I_i}]}\boldsymbol{m} = {}^{[\mathrm{I_i}]}\begin{bmatrix} u, & v \end{bmatrix}^\mathsf{T}$. Each pixel ${}^{[\Xi_\mathrm{i}]}\boldsymbol{m}$ gets associated with its cylinder's 3D point positioned at ${}^{[\mathrm{F_i}]}\mathbf{p}_{cyl_i}$, which can inherently be indicated by its elevation ${}^{[\mathrm{F_i}]}\theta_i$ and azimuth ${}^{[\mathrm{F_i}]}\psi_i$ (relative to the mirror's primary focus F_i) as illustrated in Figure 4. Thus, the ray ${}^{[\mathrm{F_i}]}\mathbf{v}_i$ of a particular 3D point directed about ${}^{[\mathrm{F_i}]}(\psi_i, \theta_i)$ must pass through P_{cyl_i} in order to get imaged as pixel ${}^{[\mathrm{I}]}\boldsymbol{m_i}$.

Since the circumference of the cylinder, w_{cyl}, is discretized with respect to the number of pixel columns or width w_Ξ, we use the pixel length l_{px} as the factor to obtain the arc length l_{ψ_i} spanned by the azimuth ${}^{[\mathrm{F_i}]}\psi_i$ out of a given ${}^{[\Xi_\mathrm{i}]}u$ coordinate on the panoramic image. Generally,

$${}^{[\mathrm{F_i}]}\psi_i = \frac{l_{\psi_i}}{r_{cyl}} = \frac{w_{cyl} - {}^{[\Xi_\mathrm{i}]}u\; l_{px}}{r_{cyl}} \tag{5.3}$$

or simply ${}^{[\mathrm{F_i}]}\psi_i = 2\pi - {}^{[\Xi_\mathrm{i}]}u\; l_{px}$ for the unit cylinder case.

An order reversal in the columns of the panorama is performed by equation (5.3) because we account for the relative position between S_{cyl_i} and the projection plane π_{img}. For $[\Xi_1]$, Figure 14 depicts the unrolling of the cylindrical panoramic image onto a planar panoramic image. Recall that the projection to the image plane However, note that π_{img} is shown from above (or its back) in Figure 14, so the panorama visualization places the viewer inside the cylinder at F_1.

Similarly, the elevation angle ${}^{[\mathrm{F_i}]}\theta_i$ is inferred out the row or ${}^{[\Xi_i]}v$ coordinate, which is scaled to its cylindrical representation by l_{px}. Recall that both cylinders have the same height, h_{cyl}, computed by equation (5.1), and by taking into account any row offset from the top or maximum height position, ${}^{[\mathrm{F_i}]}z_{cyl,max}$, of the cylinder, we get

$$ {}^{[\mathrm{F_i}]}\theta_i = \arctan\left({}^{[\mathrm{F_i}]}z_{cyl,max} - {}^{[\Xi_i]}v\; l_{px}\right) \tag{5.4} $$

Assuming coaxial alignment, out of these angles, we evaluate the positon vector ${}^{[\mathrm{C}]}\mathbf{p}_{cyl_i}$ for a point on the panoramic cylinder with respect to the camera frame [C]:

$$ {}^{[\mathrm{C}]}\mathbf{p}_{cyl_i} = \cancel{r_{cyl}} \begin{bmatrix} \cos\left({}^{[\mathrm{F_i}]}\psi_i\right) \\ \sin\left({}^{[\mathrm{F_i}]}\psi_i\right) \\ \tan\left({}^{[\mathrm{F_i}]}\theta_i\right) \end{bmatrix} + {}^{[\mathrm{C}]}\mathbf{f}_i \tag{5.5} $$

where r_{cyl} cancels out for a unit cylinder.

Therefore, we use the direction equations (5.3) and (5.4) leading to (5.5) as a process: ${}^{[\Xi_i]}\boldsymbol{m} \xmapsto[(5.4)]{(5.3)} {}^{[\mathrm{F_i}]}\begin{pmatrix}\psi\\ \theta\end{pmatrix} \xmapsto{(5.5)} {}^{[\mathrm{C}]}\mathbf{p}_{cyl_i}$, which is eventually used as the input argument to equation (3.15) in order to determine pixel ${}^{[\mathrm{I_i}]}\boldsymbol{m}$ via the mapping function $\mathbf{h}_{\Xi_i} : \mathbb{R}^2 \mapsto \mathbb{R}^2$ as following:

$$ {}^{[\mathrm{I_i}]}\boldsymbol{m} \leftarrow \mathbf{h}_{\Xi_i}\left({}^{[\Xi_i]}\boldsymbol{m}\right) := \mathbf{f}_{\varphi_i}\left({}^{[\mathrm{C}]}\mathbf{p}_{cyl_i}\big|_{{}^{[\Xi_i]}\boldsymbol{m}} \right) \tag{5.6} $$

5.1.1 Stereo Matching on Panoramas

We understand that the algorithm chosen for finding matches is crucial to attain correct pixel disparity results. We refer the reader to [4] for a detailed description of stereo correspondence methods. After comparing various block matching algorithms, we were able to obtain acceptable disparity maps with the semi-global block matching (SGBM) method introduced by [12], which can find subpixel matches in real time. As a result of this stereo block matcher among the pair of panoramic images $([\Xi_1],[\Xi_2])$, we get the dense disparity map $\left[\Xi_{\Delta \mathrm{m}_{12}}\right]$ visualized as an image in Figure 15. Note that valid disparity values must be positive (>0) and they are given with respect to the reference image, in this case, $[\Xi_1]$. In addition, recall that no stereo matching algorithm (as far as we are aware) is totally immune to mismatches due to several well-known reasons in the literature such as ambiguity of cyclic patterns.

An advantage of the block (window) search for correspondences is that it can be narrowed along epipolar lines. Unlike the traditional horizontal stereo configuration, our system captures panoramic images whose views differ in a vertical fashion. As shown in [9], the unwrapped panoramas contain vertical, parallel epipolar lines that facilitate the pixel correlation search. Thus, given a pixel position ${}^{[\Xi_1]}\boldsymbol{m}_1$ on the reference panorama $[\Xi_1]$ and its disparity value $\Delta m_{12}|_{{}^{[\Xi_1]}\boldsymbol{m}_1}$, we can resolve the correspondence ${}^{[\Xi_2]}\boldsymbol{m}_2$ pixel coordinate on the target image, $[\Xi_2]$, by simply offsetting the v-coordinate with the disparity value:

$$ {}^{[\Xi_2]}\boldsymbol{m}_2 = \begin{bmatrix} u_1 \\ v_1 + \Xi_{\Delta m_{12}}\big|_{{}^{[\Xi_1]}\boldsymbol{m}_1} \end{bmatrix} \tag{5.7} $$

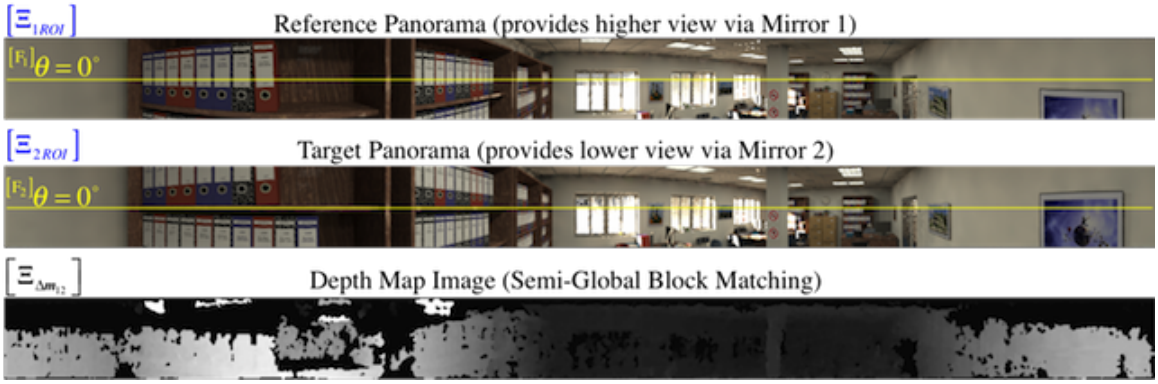
Reference Panorama (provides higher view via Mirror 1)
Target Panorama (provides lower view via Mirror 2)
Depth Map Image (Semi-Global Block Matching)

Figure 15: For the synthetic omnidirectional image [I] shown in Figure 2b, we generate its pair of panoramic images $([\Xi_1],[\Xi_2])$ using the procedure explained in Section 5.1. Note that we only work on the Stereo ROI (shown here) to perform a semi-global block match between the panoramas as indicated in Section 5.1.1. The resulting disparity map, $[\Xi_{\Delta m_{12}}]$, is visualized at the bottom as a gray-scale panoramic image normalized about its 256 intensity levels, where brighter colors imply larger disparity values. To aid the relative vertical view of both panoramas, we have annotated the row position of the zero-elevation.

5.2 Range from Triangulation

Recall the duality that states a point P_w as the intersection of a pair of lines. Regardless of the correspondence search technique employed, such as block stereo matching between panoramas $[\Xi_i]$ (Section 5.1.1) or feature detection directly on [I], we can resolve for ${}^{[I]}(\boldsymbol{m}_1,\boldsymbol{m}_2)$. From equations (3.21) and (3.28), we obtain the respective pair of back-projected rays $\left({}^{[F_1]}\mathbf{v}_1,{}^{[F_2]}\mathbf{v}_2\right)$, emanating from their respective physical viewpoints, F_1 and F_2, which are separated by baseline b. We can compute elevation angles θ_1 and θ_2 using equations (3.22) and (3.29). Then, we can triangulate the back-projected rays in order to calculate the horizontal range ρ_w defined in (3.1), as follows:

$$\rho_w = \left| \frac{b\cos(\theta_1)\cos(\theta_2)}{\sin(\theta_1-\theta_2)} \right| \tag{5.8}$$

Finally, we obtain the 3D position of P_w:

$${}^{[C]}\mathbf{p}_w = \begin{bmatrix} -\rho_w\cos(\psi_{12}) \\ -\rho_w\sin(\psi_{12}) \\ c_1-\rho_w\tan(\theta_1) \end{bmatrix} \tag{5.9}$$

where ψ_{12} is the common azimuthal angle (on the XY-plane) for coplanar rays, so it can be determined either by equation (3.23) or (3.30). Functionally, we define the "naive" intersection function that implements equation (5.9) and (5.8) such that

$${}^{[C]}\mathbf{p}_w \leftarrow \mathbf{f}_\Delta((\theta_1,\psi_1),(\theta_2,\psi_2),\boldsymbol{\theta}) \tag{5.10}$$

where $\boldsymbol{\theta}$ is the model parameters vector defined in equation (2.4) and can be omitted when calling this function because the model parameters should not change (ideally).

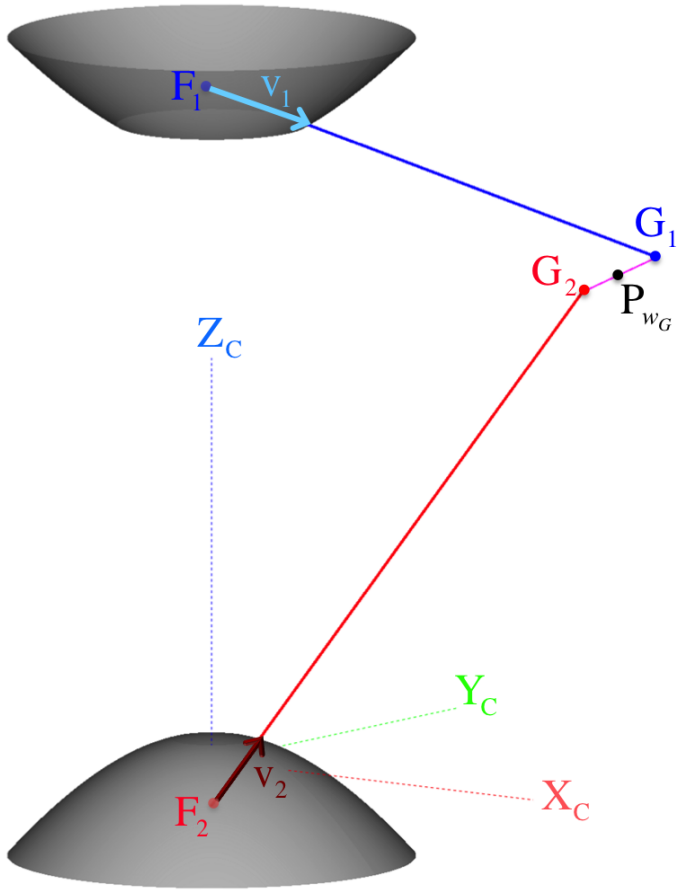

Figure 16: The more realistic case of skew back-projection rays $(\mathbf{v}_1, \mathbf{v}_2)$ approximates the triangulated point P_w by getting the midpoint P_{w_G} on the common perpendicular line segment $\overline{\mathrm{G_1G_2}} : \lambda_{1\perp 2}\hat{\mathbf{v}}_{1\perp 2}$. Note that these skey rays were formed from a pixel correspondence pair $^{[\mathrm{I}]}(\boldsymbol{m}_1, \boldsymbol{m}_2)$ and by offsetting the coordinate v_2 by 15 pixels.

5.2.1 Common Perpendicular Midpoint Triangulation Method

Because the coplanarity of these rays cannot be guaranteed (skew rays case), a better triangulation approximation while considering coaxial misalignments is to find the midpoint of their common perpendicular line segment (as attempted in [11]). As illustrated in Figure 16, we define the common perpendicular line segment $\overline{\mathrm{G_1G_2}}$ as the parametrized vector $\mathbf{v}_{1\perp 2} = \lambda_{1\perp 2}\hat{\mathbf{v}}_{1\perp 2}$, for the unit vector normal to the back-projected rays, $\mathbf{v}_1$ and $\mathbf{v}_2$, such that:

$$\hat{\mathbf{v}}_{1\perp 2} = \frac{\mathbf{v}_1 \otimes \mathbf{v}_2}{\|\mathbf{v}_1 \otimes \mathbf{v}_2\|} \tag{5.11}$$

If the rays are not parallel ($\|\mathbf{v}_1 \otimes \mathbf{v}_2\| \neq 0$), we can compute the "exact" solution, $\lambda = [\lambda_{G_1}, \quad \lambda_{G_2}, \quad \lambda_{1\perp 2}]^\mathsf{T}$, of the well-determined linear matrix equation

$$\mathbf{V}\lambda = \mathbf{b} \text{ , where } \mathbf{V} = \begin{bmatrix} \mathbf{v}_1, & -\mathbf{v}_2, & \hat{\mathbf{v}}_{1\perp 2} \end{bmatrix} \text{ and } \mathbf{b} = {}^{[\mathrm{C}]}\mathbf{f}_2 - {}^{[\mathrm{C}]}\mathbf{f}_1 \tag{5.12}$$

It follows that the location of the midpoint P_{w_G} on the common perpendicular $\mathbf{v}_{1\perp 2}$ with respect to the common frame [C] is

$${}^{[\mathrm{C}]}\mathbf{p}_{w_G} = {}^{[\mathrm{C}]}\mathbf{f}_1 + \lambda_{G_1}{}^{[\mathrm{F}_1]}\mathbf{v}_1 + \frac{1}{2}\lambda_{1\perp 2}{}^{[\mathrm{G}_1]}\hat{\mathbf{v}}_{1\perp 2} \tag{5.13}$$

5.2.2 Range Variation

Before we introduce an uncertainty model for triangulation (Section 5.3), we briefly analyze how range varies according to the possible combinations of pixel correspondences, ${}^{[\mathrm{I}]}(\boldsymbol{m}_1, \boldsymbol{m}_2)$ on the image [I]. Here, we demonstrate how a radial variation of discretized pixel disparities, Δm_{12}, affects the 3D position of a point obtained from triangulation (Section 5.2). Figure 17 demonstrates the nonlinear characteristics of the variation in horizontal range, $\Delta\rho_w$, from the discrete relation between pixel positions ${}^{[\mathrm{I}]}\boldsymbol{m}_i$ and their respective back-projected (direction) rays obtained from $\mathbf{f}_{\beta_i}$ and triangulated via function $\mathbf{f}_\Delta$ defined in (5.10). It can be observed that the horizontal range variation, $\Delta\rho_w$, increases quadratically as $\Delta m_{12} \to 1$px, which is the minimum *discrete* pixel disparity providing a maximum horizontal range $\rho_{w,max} \approx [18, 28]$ m (computed analytically). The main plot of Figure 17 shows the small disparity values in the interval $\overline{\Delta m_{12}} = [1, 20]$ px, whereas the subplot is a zoomed-in extension of the large disparity cases in the interval $\overline{\Delta m_{12}} = [20, 100]$ px.

The current analysis is an indicative that triangulation error (e.g. due to false pixel correspondences) may have a severe effect on range accuracy that increases quadratically with distance as it can be appreciated with the 8 m variation on the disparity interval $\overline{\Delta m_{12}} = [1, 2]$px Also, observe the example of Figure 20 for a reconstructed point cloud, where this range sensing characteristic is more noticeable for faraway points. In fact, the following uncertainty model provides a probabilistic framework for the triangulation error (uncertainty) that agrees with the current numerical claims.

5.3 Triangulation Uncertainty Model

Let $\mathbf{f}_{\mathrm{P}_w}$ be the vector-valued function that computes the 3D coordinates of point P_{w_G} with respect to [C] as the common perpendicular midpoint defined in equation (5.13). We express this triangulation

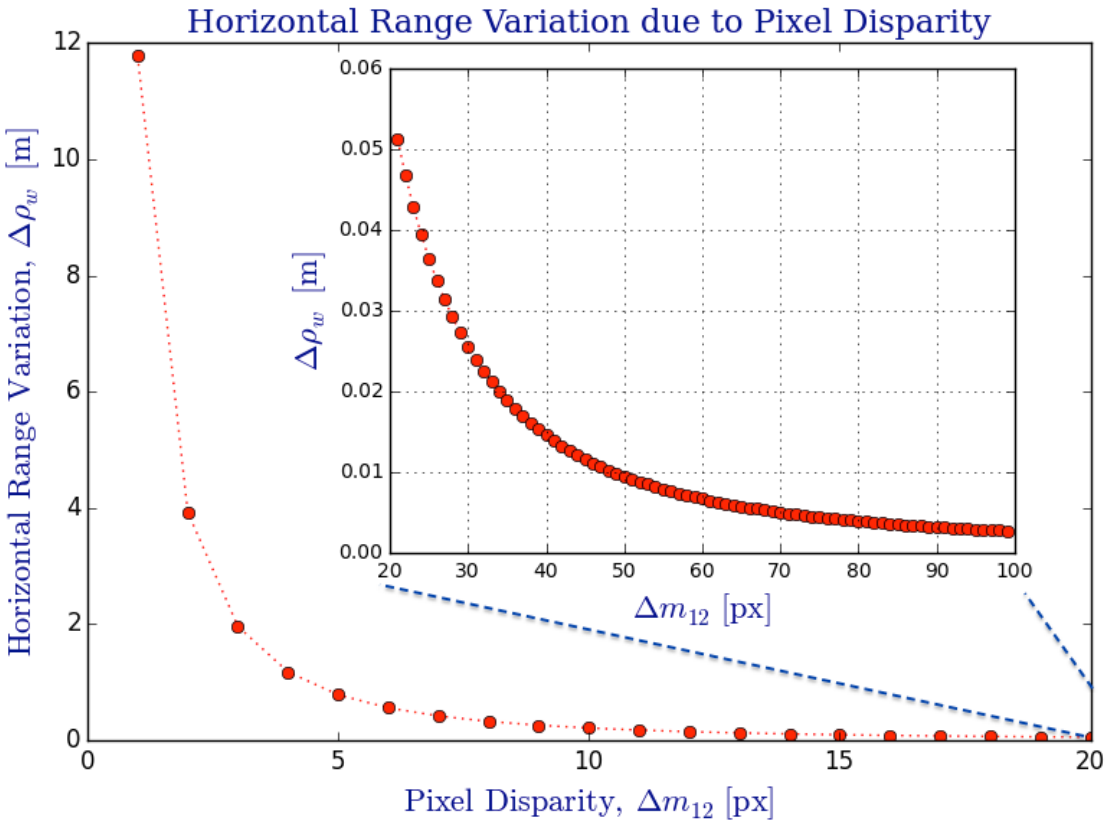
Horizontal Range Variation due to Pixel Disparity
Horizontal Range Variation, $\Delta\rho_w$ [m]
Pixel Disparity, Δm_{12} [px]
$\Delta\rho_w$ [m]
Δm_{12} [px]

Figure 17: Variation of horizontal range, $\Delta\rho_w$, due to change in pixel disparity Δm_{12} on the omnidirectional image, $[\mathrm{I}]$. There exists a "nonlinear & inverse" relation between the change in depth from triangulation ($\Delta\rho_w$) and the number of disparity pixels (Δm_{12}) available from the omnistereo image pair $([\mathrm{I}_1], [\mathrm{I}_2])$, which are exclusive subspaces of $[\mathrm{I}]$.

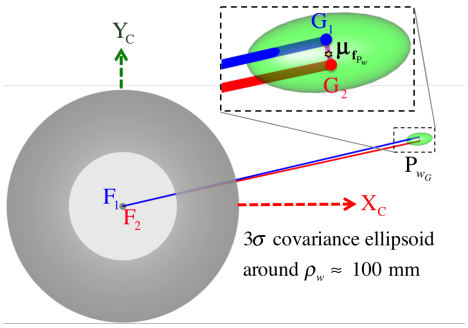

Figure 18: Top-view of the three-sigma level ellipsoid for the triangulation uncertainty of a pixel pair ${}^{[\mathrm{I}]}(\boldsymbol{m}_1, \boldsymbol{m}_2)$ with an assumed standard deviation $\sigma_{px} = 1$ px. Observe how this 1 px deviation skews the back-projected rays, so the midpoint P_{w_G} on the common perpendicular line segment $\overline{\mathrm{G}_1\mathrm{G}_2}$ is employed to estimate the mean position ${}^{[\mathrm{C}]}\boldsymbol{\mu}_{\mathbf{f}_{\mathrm{P}_w}}$ with $\rho_w \approx 100\,\mathrm{mm}$.

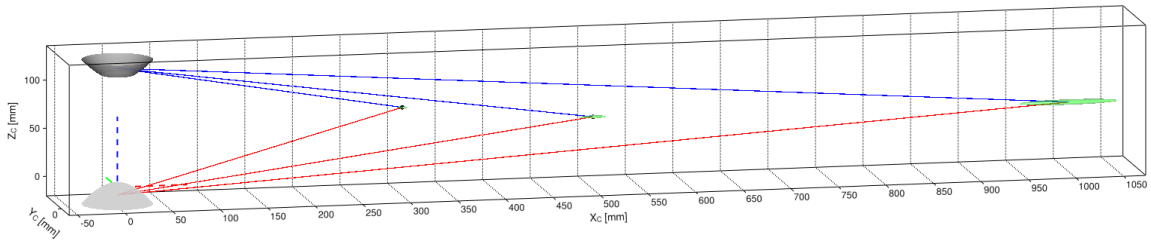

Figure 19: Visualization of a few triangulated points at mean positions ${}^{[\mathrm{C}]}\boldsymbol{\mu}_{\mathbf{f}_{\mathrm{P}_w}}$ using horizontal ranges: $\rho_w \approx \{0.3, 0.5, 1.0\}$ m and their uncertainty/error ellipsoids representing their corresponding covariance matrix $\boldsymbol{\Sigma}_{\mathbf{f}_{\mathrm{P}_w}}$ (drawn for one-$\sigma_{\mathbf{f}_{\mathrm{P}_w}}$ level and assuming $\sigma_{px} = 1$ px). Here, it is evident how the triangulation uncertainty dominates along the outward-radial direction of horizontal range ρ_w.

function component-wise as follows:

$$ {}^{[\mathrm{C}]}\mathbf{p}_{w_G} \leftarrow \mathbf{f}_{\mathrm{P}_w}(\mathbf{m}_{12}) := \begin{bmatrix} \mathrm{f}_{x_w}(\mathbf{m}_{12}) \\ \mathrm{f}_{y_w}(\mathbf{m}_{12}) \\ \mathrm{f}_{z_w}(\mathbf{m}_{12}) \end{bmatrix} \tag{5.14} $$

where $\mathbf{m}_{12} = [u_1, v_1, u_2, v_2]$ is composed by the pixel coordinates of the correspondence ${}^{[\mathrm{I}]}(\boldsymbol{m}_1, \boldsymbol{m}_2)$ upon which to base the triangulation (Section 5.2).

Without loss of generality, we model a *multivariate Gaussian* uncertainty model for triangulation, so that the position vector ${}^{[\mathrm{C}]}\mathbf{p}_{w_G}$ of any world point is centered at its mean ${}^{[\mathrm{C}]}\boldsymbol{\mu}_{\mathbf{f}_{\mathrm{P}_w}}$ with a 3×3 covariance matrix $\boldsymbol{\Sigma}_{\mathbf{f}_{\mathrm{P}_w}}$:

$$ {}^{[\mathrm{C}]}\boldsymbol{\mu}_{\mathbf{f}_{\mathrm{P}_w}} = \begin{bmatrix} x_w \\ y_w \\ z_w \end{bmatrix}, \boldsymbol{\Sigma}_{\mathbf{f}_{\mathrm{P}_w}} = \begin{bmatrix} \sigma^2_{\mathrm{f}_{x_w}} & \sigma_{\mathrm{f}_{x_w}}\sigma_{\mathrm{f}_{y_w}} & \sigma_{\mathrm{f}_{x_w}}\sigma_{\mathrm{f}_{z_w}} \\ \sigma_{\mathrm{f}_{x_w}}\sigma_{\mathrm{f}_{y_w}} & \sigma^2_{\mathrm{f}_{y_w}} & \sigma_{\mathrm{f}_{y_w}}\sigma_{\mathrm{f}_{z_w}} \\ \sigma_{\mathrm{f}_{x_w}}\sigma_{\mathrm{f}_{z_w}} & \sigma_{\mathrm{f}_{y_w}}\sigma_{\mathrm{f}_{z_w}} & \sigma^2_{\mathrm{f}_{z_w}} \end{bmatrix} \tag{5.15} $$

However, since $\mathbf{f}_{\mathrm{P}_w}$ is a non-linear vector-valued function, we linearize it by approximation to a first-order Taylor expansion and we use its Jacobian matrix to propagate the uncertainty (covariance) as in the linear case as follows:

$$ \boldsymbol{\Sigma}_{\mathbf{f}_{\mathrm{P}_w}} = \mathbf{J}_{\mathbf{f}_{\mathrm{P}_w}} \, \boldsymbol{\Omega}_{\mathbf{m}_{12}} \, {\mathbf{J}_{\mathbf{f}_{\mathrm{P}_w}}}^{\mathsf{T}} \tag{5.16} $$

where the 3×4 Jacobian matrix for the triangulation function is

$$ \mathbf{J}_{\mathbf{f}_{\mathrm{P}_w}} = \begin{bmatrix} \frac{\partial \mathrm{f}_{x_w}}{\partial u_1} & \frac{\partial \mathrm{f}_{x_w}}{\partial v_1} & \frac{\partial \mathrm{f}_{x_w}}{\partial u_2} & \frac{\partial \mathrm{f}_{x_w}}{\partial v_2} \\ \frac{\partial \mathrm{f}_{y_w}}{\partial u_1} & \frac{\partial \mathrm{f}_{y_w}}{\partial v_1} & \frac{\partial \mathrm{f}_{y_w}}{\partial u_2} & \frac{\partial \mathrm{f}_{y_w}}{\partial v_2} \\ \frac{\partial \mathrm{f}_{z_w}}{\partial u_1} & \frac{\partial \mathrm{f}_{z_w}}{\partial v_1} & \frac{\partial \mathrm{f}_{z_w}}{\partial u_2} & \frac{\partial \mathrm{f}_{z_w}}{\partial v_2} \end{bmatrix} \tag{5.17} $$

and the $4x4$ covariance matrix of the pixel arguments being

$$ \boldsymbol{\Omega}_{\mathbf{m}_{12}} = \sigma^2_{px}\mathbf{I}_4 \tag{5.18} $$

where we assume $\sigma_{px} = 1$ px for the standard deviation of each pixel coordinate in the *discretized* pixel space. The complete symbolic solution of $\boldsymbol{\Sigma}_{\mathbf{f}_{\mathrm{P}_w}}$ is too involved to appear in this manuscript. However, in Figure 18, we show the top-view of the covariance ellipsoid drawn at a three-$\sigma_{\mathbf{f}_{\mathrm{P}_w}}$ level for a point triangulated nearly around $\rho_w \approx 100\,\mathrm{mm}$. Figure 19 visualizes uncertainty ellipsoids drawn at a one-$\sigma_{\mathbf{f}_{\mathrm{P}_w}}$ level for several triangulation ranges. We refer the reader to the end of Section 6.1.1 where we validate this safe assumption through experimental results using subpixel precision.

6 Experiment Results and Future Work

6.1 3D Sensing Results

By implementing the process described in Section 5, we attempt to reconstruct the 3D scene (as a point-cloud) obtained from the omnidirectional synthetic image given in Figure 2b, whose actual

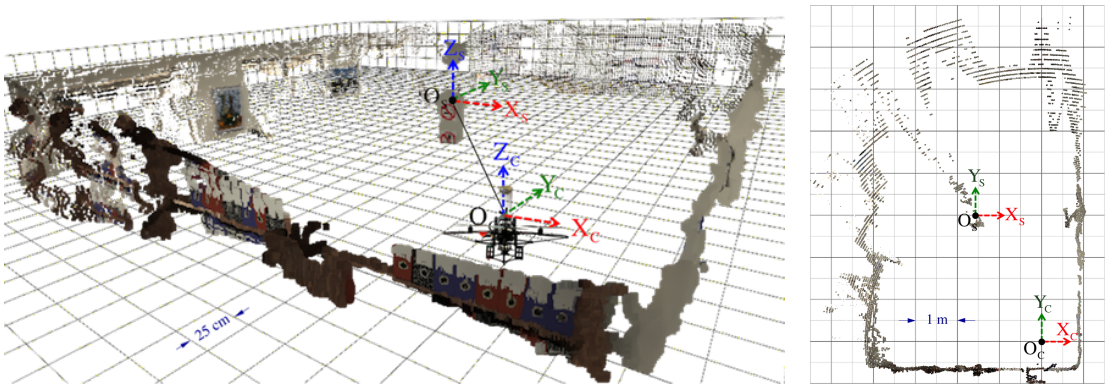

(a) 3D Perspective View **(b)** Orthographic View

Figure 20: A 3-D dense point cloud computed out of the synthetic model that rendered the omnidirectional image shown in Figure 2b. Pixel correspondences are established via the panoramic depth map visualized in Figure 15. The 3D point triangulation implements the common perpendicular midpoint method indicated in Section 5.2.1. The position of the omnistereo sensor mounted on the quadrotor is annotated as frame [C] with respect to the scene's coordinates frame [S]. **(a)** 3D visualization of the point cloud (the quadrotor with the omnistereo rig has been added for visualization only). **(b)** Orthographic projection of the point cloud to the XY-plane of the visualization grid.

size is 1280x960 pixels. The associated panoramic images, $[\Xi_i]$, were obtained using function $\mathbf{h}_{\Xi_i}$ defined in equation (5.6) and are shown in Figure 15. In fact, the point-cloud are generated using the dense stereo "template matching" technique discussed in Section 5.1.1 and its resulting depth map is shown here, too. Pixel correspondences $({}^{[\Xi_1]}\boldsymbol{m}_1, {}^{[\Xi_2]}\boldsymbol{m}_2)$ on the panoramic representations are mapped via $\mathbf{h}_{\Xi_i}$ into their respective image positions ${}^{[I]}(\boldsymbol{m}_1, \boldsymbol{m}_2)$. Then, these are triangulated with ${}^{[C]}\mathbf{f}_{P_w}$ given in equation (5.14), resulting in the set (cloud) of color 3D points P_Δ visualized in Figure 20. Here, the synthetic scene (Figure 2a) is for a room 5.0 m wide (along its X-axis), 8.0 m long (along its Y-axis), and 2.5 m high (along its Z-axis). With respect to the scene center of coordinates, [S], the catadioptric omnistereo sensor, [C], is positioned at ${}^{[S]}_{[C]}\mathbf{t} = [1.60, \quad -2.85, \quad 0.16]^\mathsf{T}$ in meters.

Finally, we present some preliminary results from a real experiment using the prototype described in Section 4.3.2 and shown in Figure 13a. The panoramic images and point cloud shown in Figure 21 are obtained by implementing the pertinent functions described throughout this manuscript and by holding the SVP assumption of an ideal configuration. Merely, we provide these results as proof of concept and we are aware that an adequate calibration procedure for the proposed omnistereo sensor is desired.

6.1.1 Sparse Triangulation Root-Mean-Square Error

Due to the unstructured nature of the dense point clouds previously discussed, we proceed to triangulate sets of sparse 3D points whose poses with respect to the omnistereo sensor camera frame, [C], are known in advance. For various predetermined poses ${}^{[C]}_{[G]}\mathbf{T}_h$, we synthetize a chessboard

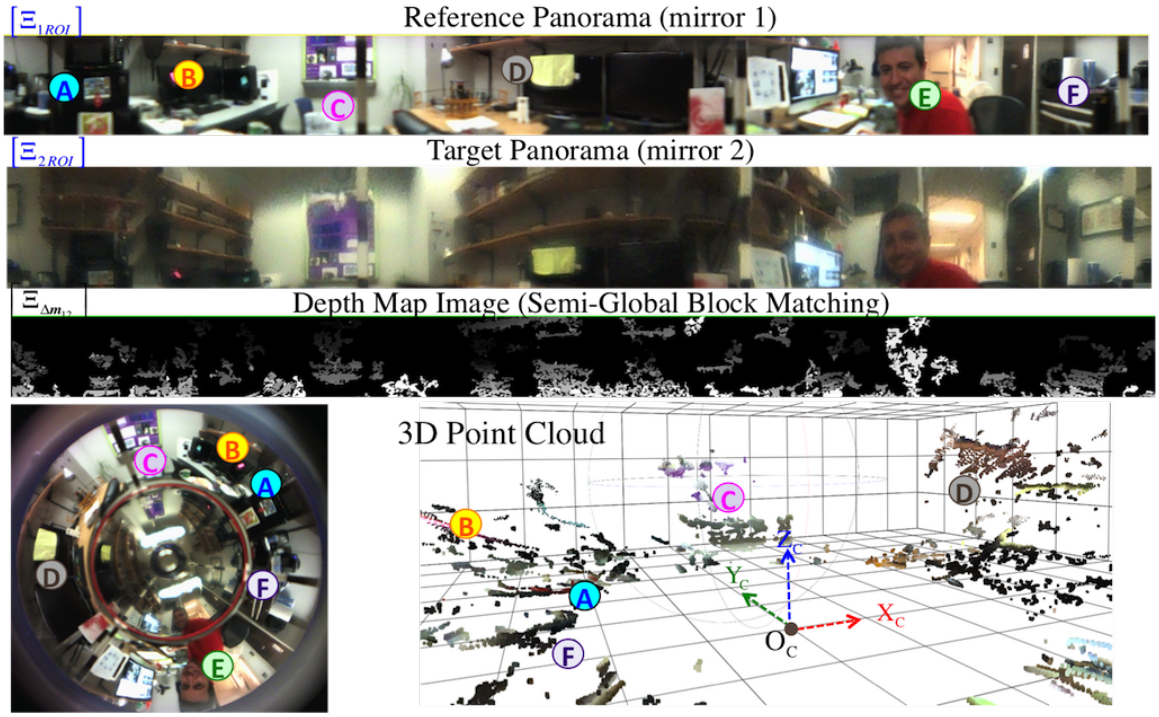

Figure 21: Real-life experiment using the 37 mm-radius prototype and a single 2592x1944 pixels image (catadioptric view) from its color monocular camera. The rig was positioned in the middle of the room observed in Figure 13a. These panoramic images and depth map were obtained using the same procedure implemented for the synthetic model experiment. In order to better appreciate the resulting 3D point cloud, we have exagerated the point size and annotated several landmarks around the scene:
Ⓐ Appliances, Ⓑ left desktop, Ⓒ back wall, Ⓓ right desktop, Ⓔ person, Ⓕ toolbox. The grid size spacing is 0.50 m in all directions.

Table 4: Results of RMSE from Triangulation Experiment

${}^{[C]}\rho_{O_G}$ [m]	RMSE [mm]	SD [mm]
0.25	0.46	0.31
0.50	1.20	0.71
1.0	4.62	2.55
2.0	14.85	9.06
4.0	57.67	31.34
8.0	219.09	129.92

calibration frame [G] containing $m \times n$ square cells. Since the sensor is assumed to be rotationally symmetric, it suffices to experiment with groups of 4 chessboard patterns situated at a given horizontal range. A total of $4mn$ 3D points are available for each range group. Each corner point's position ${}^{[C]}\mathbf{p}_j$ is found with respect to [C] via the frame transformation ${}^{[C]}\mathbf{p}_j = {}^{[C]}_{[G]}\mathbf{T}_h {}^{[G]}\mathbf{p}_j$ for all indices $j \in \{1,\ldots,4mn\}$.

Figure 22 shows the set of detected corner points from the group of patterns set to ${}^{[C]}\rho_{O_G} = 2\,\text{m}$. We adjust the pattern's cell sizes accordingly so its points can be safely discerned by an automated corner detector [4]. We systematically establish correspondences of pattern points on the omnidirectional image, and proceed to triangulate with equation (5.14). For each range group of points, we compute the root-mean-square of the 3D position errors (RMSE) between the observed (triangulated) points ${}^{[C]}\tilde{\mathbf{p}}_j \leftarrow \mathbf{f}_{P_w}(\tilde{\boldsymbol{m}}_1, \tilde{\boldsymbol{m}}_2)$ and the true (known) points ${}^{[C]}\mathbf{p}_j$ that were used to describe the ray-traced image. Table 4 compiles the RMSE results and the standard deviation (SD) for some group of patterns with origin, O_G, located at specified horizontal ranges ${}^{[C]}\rho_{O_G} \in [0.25, 8.0]$ m away.

Finally, we notice that for all the 3D points in the patterns, we obtained an average error of 0.1 px with a standard deviation $\tilde{\sigma}_{px} = 0.05$ px for the subpixel detection of corners on the image versus their theoretical values obtained from $\mathbf{f}_{\varphi_i}$ defined in (3.15). This last experiment helps us validate the pessimistic choice of $\sigma_{px} = 1$ px for the discrete pixel space in the triangulation uncertainty model proposed in Section 5.3.

6.2 Discussion and Future Work

The portable aspect of the proposed omnistereo sensor is one of its greatest advantages (as discussed in the introduction section). The total weight of the big rig using 37 mm-radius mirrors is about 550 g, so it can be carried by the AscTec Pelican quadrotor under its payload limitations of 650 g. The mirror profiles have been optimized for the maximization of the stereo baseline while obeying the various design constraints such as size and field of view. Currently, the mirrors are custom-manufactured out of brass using a CNC machine, and they seem to meet the performance specifications (e.g., FOV, resolution). We are hoping to reduce the system's weight dramatically by employing aluminum or plastic-based mirrors.

In reality, it is almost impossible to assemble a perfect imaging system that fulfills the SVP

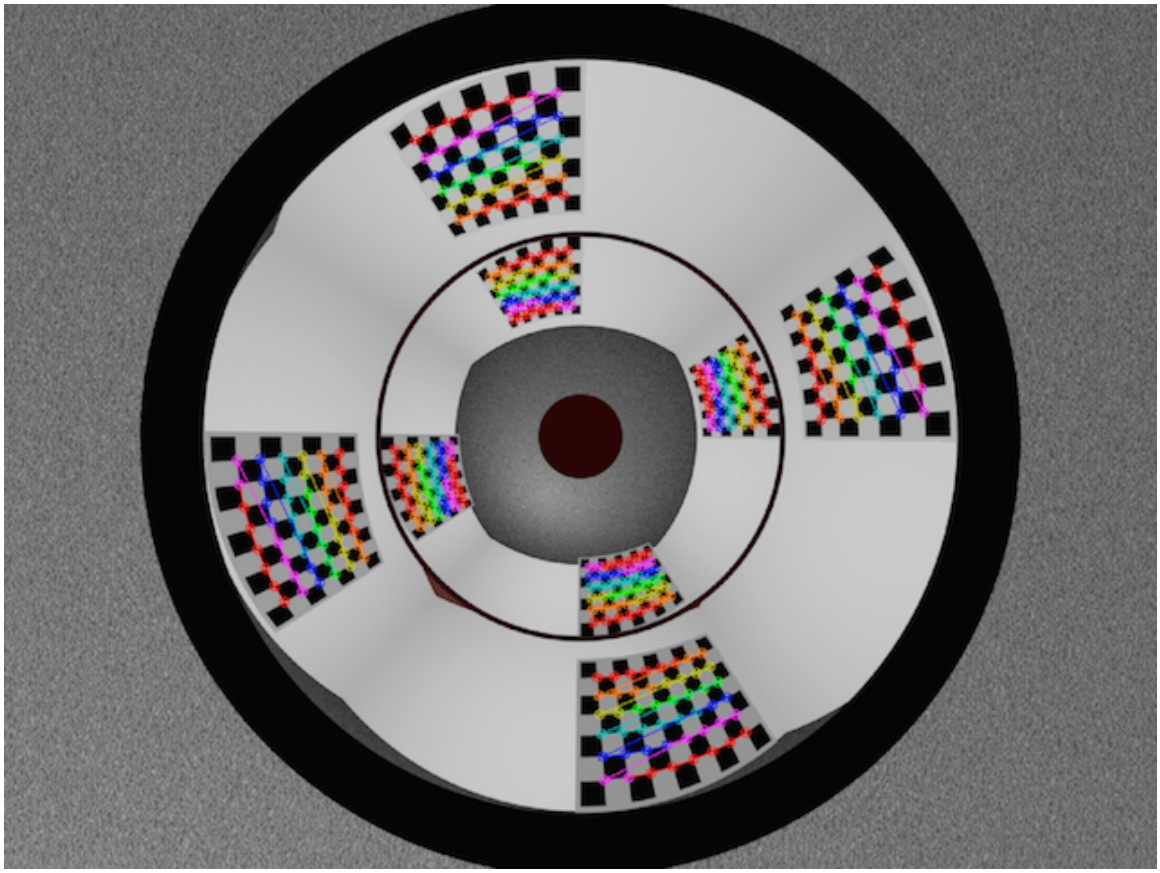

Figure 22: Example of sparse point correspondences detected from intersecting corners on chessboard patterns around the omnistereo sensor. The size of the rendered images for this experiment is 1280x960 pixels, and the cell size for this example's patterns is 140 mm $\times$ 140 mm. The RMSE of this set of pattern points with origin points at ${}^{[C]}\rho_{O_G} = 2\,\text{m}$ is approximately 15 mm given in Table 4 and using a subpixel precision corner detector.

assumption and avoids the triangulation uncertainty studied in Section 5.3 on top of the error already introduced by any feature matching technique. The coaxial misalignment of the folded mirrors-camera system, defocus blur of the lens, and the inauspicious glare from the support tube are all practical caveats we need to overcome for better 3D sensing tasks. In fact, we avoided using the tube in our real-life experiment. The eminent need for an omnistereo calibration tool is part of our near future endeavors.

The ongoing research is also focusing on the development of efficient software algorithms for real-time 3D pose estimation and scene reconstruction via dense or sparse point clouds as to fit a particular application. Bear in mind that all the experimental results demonstrated in this manuscript rely upon a single camera snapshot. We understand that the narrow vertical field-of-view where stereo vision operates is a limiting factor for dense scene reconstruction from a single image. However, we believe that robust feature tracking can lead to a robust pose estimation procedure by gathering key point features all around the sensor. As in our past work [18], the possibility of fusing multiple modalities (e.g. stereo and optical-flow) is possible in order to resolve the scale-factor problem inherent in the single, non-overlapping views.

In this work, we have validated the accuracy of synthetic experiments (in the ideal case), in addition to an extensive study of the sensor's properties, such as its spatial resolution. In order to validate the precision of the real sensor, we would require ground truth data obtained from a relative position reference system, which we don't have at the moment. Our ultimate goal is to apply the omnistereo sensor for autonomous flight using algorithms running on-board the quadrotor's embedded computer. 3D simultaneous localization and mapping (SLAM) using the omnistereo vision system will be integrated with our current autonomous navigation framework demonstrated in [30]. At large, we have presented a thorough geometrical model and analytical solution to a useful omnistereo sensor. We are willing to provide the corresponding software components upon request until the final versions get implemented and released to the public.

References

[1] Zafer Arcan, Pascal Frossard, and Z. Arican. Dense Depth Estimation from Omnidirectional Images. *Journal of Computer Vision and Image Understanding*, 2009.

[2] Ruzen Bajcsy and Shih-Schon Lin. High resolution catadioptric omni-directional stereo sensor for robot vision. In *2003 IEEE International Conference on Robotics and Automation (Cat. No.03CH37422)*, pages 1694–1699. Ieee, 2003.

[3] Simon Baker and Shree K. Nayar. A theory of single-viewpoint catadioptric image formation. *International Journal of Computer Vision*, 35(2):175–196, 1999.

[4] G. Bradski and A. Kaehler. *Learning OpenCV: Computer vision with the OpenCV library*. O'Reilly Media, 2008.

[5] Jeffrey Byrne, Martin Cosgrove, and Raman Mehra. Stereo based obstacle detection for an unmanned air vehicle. In *International Conference on Robotics and Automation*, 2006.

[6] Eduardo E.L.L. Cabral, José C. Junior de Souza, and Marcos C Hunold. Omnidirectional stereo vision with a hyperbolic double lobed mirror. In *Proceedings of the 17th International Conference on Pattern Recognition (ICPR)*, pages 0–3. Ieee, 2004.

[7] Anders Forsgren, PE Gill, and MH Wright. Interior Methods for Nonlinear Optimization. *Society for Industrial and Applied Mathematics (SIAM Review)*, 44(4):525–597, 2002.

[8] Jose Gaspar, Claudia Deccó, Jun Jr. Okamoto, Jose Santos-Victor, Instituto De Sistemas, Av Rovisco Pais, and S P Brazil. Constant resolution omnidirectional cameras. In *OMNIVIS'02 Workshop on Omni-directional Vision*, 2002.

[9] Joshua Gluckman, Shree K. Nayar, and Keith KJ Keith J. Thoresz. Real-Time Omnidirectional and Panoramic Stereo. *Computer vision and image understanding*, 1998.

[10] Ling Guo, Igor Labutov, Jizhong Xiao, and Senior Member. Design and calibration of single-camera catadioptric omnistereo system for miniature aerial vehicles (MAVs). *IEEE/RSJ International Conference on Intelligent Robots and Systems (IROS)*, 1003, 2010.

[11] Lei He, Chuanjiang Luo, Feng Zhu, and Yingming Hao. Stereo Matching and 3D Reconstruction via an Omnidirectional Stereo Sensor. In *Motion Planning*, number 60575024, pages 123–142. In-Tech Education and Publishing, Vienna, Austria, 2008.

[12] Heiko Hirschmüller. Stereo processing by semiglobal matching and mutual information. *IEEE transactions on pattern analysis and machine intelligence*, 30(2):328–41, February 2008.

[13] Stefan Hrabar. 3D path planning and stereo-based obstacle avoidance for rotorcraft UAVs. *IEEE/RSJ International Conference on Intelligent Robots and Systems (IROS)*, pages 807–814, September 2008.

[14] Stefan Hrabar and GS Sukhatme. Omnidirectional vision for an autonomous helicopter. In *International Conference on Robotics and Automation (ICRA)*, number April, pages 3602–3609, 2003.

[15] Gijeong Jang, Sungho Kim, and Inso Kweon. Single camera catadioptric stereo system. In *Proceedings of Workshop on Omnidirectional Vision, Camera Networks and Nonclassical cameras (OMNIVIS2005)*. Citeseer, 2005.

[16] Carlos Jaramillo, Ling Guo, and Jizhong Xiao. A Single-Camera Omni-Stereo Vision System for 3D Perception of Micro Aerial Vehicles (MAVs). In *IEEE Conference on Industrial Electronics and Applications (ICIEA)*, volume 10016, 2013.

[17] Hiroshi Koyasu, Jun Miura, and Yoshiaki Shirai. Realtime omnidirectional stereo for obstacle detection and tracking in dynamic environments. In *International Conference on Intelligent Robots and Systems (IROS)*, volume 1, pages 31–36, Maui, Hawaii, 2001.

[18] Igor Labutov, Carlos Jaramillo, and Jizhong Xiao. Generating near-spherical range panoramas by fusing optical flow and stereo from a single-camera folded catadioptric rig. *Machine Vision and Applications*, 24(1):1–12, September 2011.

[19] El Mustapha Mouaddib and Ryusuke Sagawa. Stereovision with a single camera and multiple mirrors. *International Conference on Robotics and Automation*, (April):800–805, 2005.

[20] Shree K. Nayar and Simon Baker. Catadioptric Image Formation. In *Proceedings of the 1997 DARPA Image Understanding Workshop*, pages 1431–1437, 1997.

[21] Shree K. Nayar and Venkata Peri. Folded catadioptric cameras. *Proceedings. 1999 IEEE Computer Society Conference on Computer Vision and Pattern Recognition (Cat. No PR00149)*, pages 217–223, 1999.

[22] M Schönbein, B Kitt, and M Lauer. Environmental Perception for Intelligent Vehicles Using Catadioptric Stereo Vision Systems. In *In Proc. of the European Conference on Mobile Robots (ECMR)*, pages 1–6, 2011.

[23] L. Smadja, R. Benosman, and J. Devars. Hybrid stereo configurations through a cylindrical sensor calibration. *Machine Vision and Applications*, 17(4):251–264, 2006.

[24] Libor Spacek. Coaxial Omnidirectional Stereopsis. *Computer Vision-ECCV 2004*, pages 354–365, 2004.

[25] Peter Sturm, Srikumar Ramalingam, Jean-Philippe Tardif, Simone Gasparini, and Joao P Barreto. Camera models and fundamental concepts used in geometric computer vision. *Foundations and Trends in Computer Graphics and Vision*, 6(1-2):1–183, 2011.

[26] Liancheng Su and Feng Zhu. Design of a novel stereo vision navigation system for mobile robots. In *IEEE Robotics and Biomimetics (ROBIO)*, pages 611–614, 2005.

[27] Rahul Swaminathan, Michael D. Grossberg, and Shree K. Nayar. Caustics of catadioptric cameras. *Proceedings Eighth IEEE International Conference on Computer Vision. ICCV 2001*, 2:2–9, 2001.

[28] Ascending Technologies. AscTec Pelican.

[29] Tinne Tuytelaars Tuytelaars and Krystian Mikolajczyk. Local Invariant Feature Detectors- A Survey. *Foundations and Trends in Computer Graphics and Vision*, 3(3):177–280, 2008.

[30] Roberto G Valenti, Ivan Dryanovski, Carlos Jaramillo, Daniel Perea Strom, and Jizhong Xiao. Autonomous quadrotor flight using onboard RGB-D visual odometry. In *International Conference on Robotics and Automation (ICRA 2014)*, pages 5233 – 5238, 2014.

[31] Sooyeong Yi and N. Ahuja. An Omnidirectional Stereo Vision System Using a Single Camera. *18th International Conference on Pattern Recognition (ICPR'06)*, pages 861–865, 2006.